

Mechanics of Advanced Materials and Structures



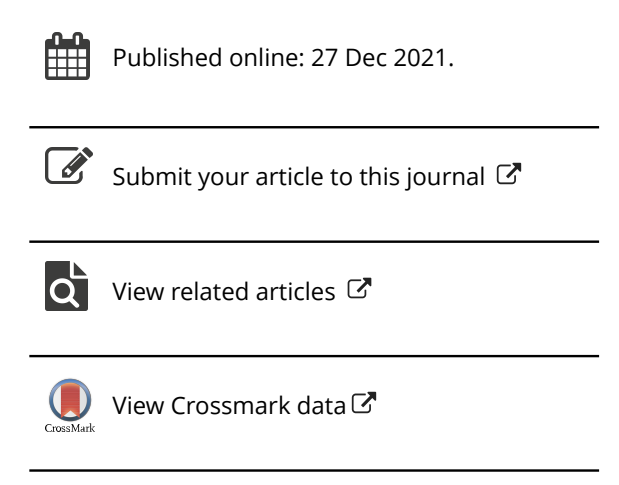
ISSN: (Print) (Online) Journal homepage: https://www.tandfonline.com/loi/umcm20

Optimal local truncation error method for solution of elasticity problems for heterogeneous materials with irregular interfaces and unfitted Cartesian meshes

A. Idesman, B. Dey & M. Mobin

To cite this article: A. Idesman, B. Dey & M. Mobin (2021): Optimal local truncation error method for solution of elasticity problems for heterogeneous materials with irregular interfaces and unfitted Cartesian meshes, Mechanics of Advanced Materials and Structures, DOI: 10.1080/15376494.2021.2014001

To link to this article: https://doi.org/10.1080/15376494.2021.2014001





ORIGINAL ARTICLE



Optimal local truncation error method for solution of elasticity problems for heterogeneous materials with irregular interfaces and unfitted Cartesian meshes

A. Idesman^a, B. Dey^b, and M. Mobin^a

^aDepartment of Mechanical Engineering, Texas Tech University, Lubbock, Texas, USA; ^bDepartment of Mechanical Engineering, University of Utah, Salt Lake City, Utah, USA

ABSTRACT

The optimal local truncation error method (OLTEM) with unfitted Cartesian meshes was recently developed for PDEs with homogeneous materials on regular and irregular domains as well as for the scalar time-dependent wave and heat equations for heterogeneous materials with irregular interfaces. Here, OLTEM is extended to a system of time-independent elastic PDEs for heterogeneous materials with irregular interfaces and unfitted Cartesian meshes. We show the development of OLTEM for the 2D elasticity equations using compact 9-point stencils that are similar to those for linear quadrilateral finite elements. The interface conditions on the interfaces where the jumps in material properties occur are added to the expression for the local truncation error and do not change the width of the stencils. There are no unknowns on interfaces between different materials; the structure of the global discrete equations is the same for homogeneous and heterogeneous materials. The calculation of the unknown stencil coefficients is based on the minimization of the local truncation error of the stencil equations and yields the optimal second order of accuracy for OLTEM with 9-point stencils on unfitted Cartesian meshes. Numerical experiments for elastic heterogeneous materials with irregular interfaces show that at the same number of degrees of freedom: a) OLTEM with unfitted Cartesian meshes is more accurate than linear finite elements with similar stencils and conformed meshes; b) up to engineering accuracy of 1%, OLTEM with unfitted Cartesian meshes is even more computationally efficient than quadratic and cubic finite elements with much wider stencils and conformed meshes. The proposed technique yields accurate numerical results for heterogeneous materials with big contrasts in the material properties of different components. Due to the computational efficiency and trivial unfitted Cartesian meshes that are independent of irregular geometry, the proposed technique does not require remeshing for the shape change of irregular geometry and it will be effective for many design and optimization problems.

ARTICLE HISTORY

Received 15 September 2021 Accepted 30 November 2021

KEYWORDS

Elasticity equations for heterogeneous materials; irregular interfaces; local truncation error; unfitted Cartesian meshes; optimal accuracy

1. Introduction

The finite element method, the finite volume method, the isogeometric elements, the spectral elements, and similar techniques represent very powerful tools for the solution of partial differential equations (PDEs) for a complex geometry. However, the generation of non-uniform meshes for a complex geometry is not simple and may lead to the decrease in accuracy of these techniques if 'bad' elements (e.g., elements with small angles) appear in the mesh. Moreover, the conventional derivation of discrete equations for these techniques (e.g., based on the Galerkin approaches) does not lead to the optimal accuracy. There is a significant number of publications related to the numerical solution of different PDEs on irregular domains with uniform embedded meshes. For example, we can mention the following fictitious domain numerical methods that use uniform embedded meshes: the embedded finite difference method, the cut finite element method, the finite cell method, the Cartesian grid method, the immersed interface method, the virtual

boundary method, the embedded boundary method, etc.; e.g., see [1-30] and many others. The main objective of these techniques is to simplify the mesh generation for irregular domains as well as to mitigate the effect of 'bad' elements. For example, the techniques based of the finite element formulations (such as the cut finite element method, the finite cell method, the virtual boundary method, and others) yield the p+1 order of accuracy even with small cut cells generated due to complex irregular boundaries (e.g., see [2-5,9,28,29] and many others). The main advantage of the embedded boundary method developed in the articles [10-12,23,25] is the use of simple Cartesian meshes. The boundary conditions or fluxes in this technique are interpolated using the Cartesian grid points and this leads to the increase in the stencil width for the grid points located close to the boundary (the numerical techniques developed in the articles [10-12,24,25] provide just the second order of accuracy for the global solution). A stable generalized finite element method for the Poisson equation was developed in the article [31] for heterogeneous materials with curved interfaces and unfitted uniform meshes. The second order of accuracy in the energy norm was achieved in the article [31] with 2D quadratic finite elements that form 25-point stencils. The development of different numerical techniques (finite difference method, immersed finite element method, and immersed meshfree method) for elasticity interface problems with unfitted meshes was recently reported in the articles [32-34]. For example, unfitted meshes in the article [32] lead to the increase in the stencil widths for the grid points located close to the irregular interfaces as well as to some difficulties with the finite difference approximations of the derivatives used in the interface conditions. For the immersed finite element method in the article [33], the second order of accuracy is reached with a larger number of degrees of freedom in the stencil equation compared to that for the approach proposed in this article. The immersed meshfree method in the article [34] provides a low order of convergence (smaller than two) for the problem with a circular inclusion (a similar problem is considered in Section 3).

The development of robust numerical techniques for the solution of PDEs for heterogeneous materials with complex irregular interfaces that provide an optimal accuracy on simple unfitted meshes is still a challenging problem.

Recently in these articles [35-41], OLTEM has been developed for the solution of PDEs with constant coefficients on regular and irregular domains with Cartesian meshes. At the same structure of the semidiscrete or discrete equations, the new technique provides the optimal order of accuracy that exceeds the order of accuracy of many known numerical approaches on regular and irregular domains. For example, in our article [35], it was shown that OLTEM with 9-point stencils (similar to those for linear finite elements) provides the second order of accuracy for the 2D elasticity on regular domains. The second order of accuracy is the optimal accuracy for all 9-point stencils independent of the numerical method used for their derivations. Our article [35] also shows that OLTEM with 25-point stencils (similar to those for quadratic finite elements) provides the 10th order of accuracy for the 2D elasticity on regular domains. In our article [36], we have extended OLTEM with 9-point stencils (similar to those for linear finite elements) and unfitted Cartesian meshes to a much more general case of the 2D time-dependent scalar heat and wave equations with discontinuous coefficients and we have obtained the third order of accuracy of the new approach.

Here, we continue the development of OLTEM for heterogeneous materials with irregular interfaces started in our article [36] and we consider the development of OLTEM with 9-point stencils (similar to those for linear elements) and unfitted Cartesian meshes for a system of the 2D time-independent elasticity equations with discontinuous coefficients. In contrast to our article [36] where the additional time derivatives of the interface conditions are used for the derivation of OLTEM and where the time derivatives in the local truncation error are replaced by the space derivatives, the time-independent elasticity equations do not include the time variable and the derivation of OLTEM for the elasticity

is different from that in our article [36]. Even the stencil equations are the ordinary differential equations in our article [36] but they are the algebraic equations in this article. We should also mention that in contrast to our article [36] where OLTEM with 9-point stencils for one scalar PDE (the heat or wave equation) provides the third order of accuracy, OLTEM with 9-point stencils for two elasticity PDEs simultaneously used for the derivation of the stencil coefficients provides the second order of accuracy. Nevertheless, due to the minimization of the leading terms of the local truncation error, up to engineering accuracy of 1%, OLTEM with unfitted Cartesian meshes is even more computationally effective than quadratic and cubic finite elements with much wider stencils and conformed meshes.

The idea of OLTEM for the solution of PDEs is very simple. First, an unfitted Cartesian mesh is selected independent of the irregular domain under consideration. Then, stencil equations of a discrete system are assumed for all internal grid points of the Cartesian mesh located inside the domain. The stencil equation for each internal grid point is a linear combination of the numerical values of the unknown functions at a number of grid points included into the stencil; e.g., see Eq. (8) below. The stencil equations for all internal grid points form the global discrete system of equations for OLTEM. The coefficients of the stencil equations are assumed to be unknown. These unknown coefficients are determined by the minimization of the order of the local truncation error for each stencil equation. This procedure includes a Taylor series expansion of the unknown exact solution at the grid points and its substitution into the stencil equation. As a result, we obtain the local truncation error in the form of a Taylor series. At this point, no information about PDEs is used. Then, the corresponding PDEs are applied at the grid points in order to exclude some partial derivatives in the expression for the local truncation error. Finally, the unknown coefficients of each stencil equation are calculated from a small local system of algebraic equations. This local system is obtained by equating to zero the lowest terms in the Taylor series expansion of the local truncation error and by the minimization of the non-zero leading terms of the local truncation error with the least square method. The coefficients of the stencil equations are similarly calculated for homogeneous (no interfaces) stencils and for heterogeneous (with interfaces) stencils. The heterogeneous stencils additionally include the known interface conditions at a small number of selected interface points located on the irregular interface. There are no unknowns at the interface points. Finally, a fully discrete global system with unknowns at the internal grid points can be easily solved. The structure of this system is the same for homogeneous and heterogeneous materials (the difference is in the values of the stencil coefficients). The main advantages of OLTEM are an optimal accuracy and the simplicity of the formation of a discrete system for irregular interfaces with unfitted Cartesian meshes. Changing the width of the stencil equations, different linear and high-order numerical techniques can be developed.

The focus of this article is the development of 2D compact 9-point stencils (similar to those for linear elements) affected by irregular interfaces between different elastic materials with simple unfitted Cartesian meshes.

The 2D time-independent elasticity equations in a composite domain $\Omega = \bigcup \Omega_l$ $(l = 1, 2, ..., \bar{N}$ where \bar{N} is the total number of subdomains) can be written down in each subdomain Ω_l as follows:

$$\mu_{l}\nabla^{2}u_{l} + (\mu_{l} + \lambda_{l})\left(\frac{\partial^{2}u_{l}}{\partial x^{2}} + \frac{\partial^{2}v_{l}}{\partial x\partial y}\right) + f_{x}^{l} = 0 ,$$

$$\mu_{l}\nabla^{2}v_{l} + (\mu_{l} + \lambda_{l})\left(\frac{\partial^{2}v_{l}}{\partial y^{2}} + \frac{\partial^{2}u_{l}}{\partial x\partial y}\right) + f_{y}^{l} = 0 ,$$

$$(1)$$

where $u_l = u_l(x, y)$ and $v_l = v_l(x, y)$ are the x- and y- components of the displacement vector, $f_x^l = f_x^l(x, y)$ and $f_y^l =$ $f_{\nu}^{l}(x,y)$ are the x- and y- components of the body forces that can be discontinuous across interfaces, μ_l and λ_l are Lame coefficients that can be also expressed in terms of Young's modulus E and Poisson's ratio ν as follows:

$$\mu_l = \frac{E_l}{2(1+\nu_l)}$$
, $\lambda_l = \frac{E_l \nu_l}{(1+\nu_l)(1-2\nu_l)}$. (2)

We also assume that the functions u_l and f_l are sufficiently smooth in each subdomain Ω_l . At the interface G between any two subdomains, the following interface conditions (the continuity of the displacements and the tractive forces across the interface) are applied:

$$u_G^* - u_G^{**} = 0$$
, $v_G^* - v_G^{**} = 0$, (3)

$$t_{x,G}^* - t_{x,G}^{**} = 0$$
 , $t_{y,G}^* - t_{y,G}^{**} = 0$, (4)

where the symbols * and ** correspond to the quantities on the opposite sides from the interface for the corresponding subdomains Ω_l . The the x- and y- components of the tractive forces $t_{x,G}$ and $t_{y,G}$ can be expressed in terms of the displacements as follows:

$$t_{x,G} = n_x \left[(\lambda + 2\mu) \frac{\partial u}{\partial x} + \lambda \frac{\partial v}{\partial y} \right] + n_y \mu \left(\frac{\partial u}{\partial y} + \frac{\partial v}{\partial x} \right) ,$$

$$t_{y,G} = n_y \left[(\lambda + 2\mu) \frac{\partial v}{\partial y} + \lambda \frac{\partial u}{\partial x} \right] + n_x \mu \left(\frac{\partial u}{\partial y} + \frac{\partial v}{\partial x} \right) ,$$

where n_x and n_y are the x and y components of the normal vector at the interface. According to Eqs. (3)-(5), the displacements u and v are continuous across the interfaces but they can have the discontinuous spatial derivatives across the interfaces.

Remark 1. The derivation of the new approach can be easily extended to the case with the discontinuous displacements and tractive forces across interfaces; i.e., when the righthand sides in Eqs. (3) and (4) are the given functions. However, for simplicity, we consider Eqs. (3) and (4) with zero right-hand sides.

In this article, the Dirichlet boundary conditions $u = g_1$ and $v = g_2$ are applied along the external boundary Γ where g_1 and g_2 are the given functions. However, the Neumann boundary conditions (tractive forces) can be also used with the proposed approach; e.g., see our articles [37,38]. According to OLTEM, the discrete system for the elasticity equations, Eq. (1), after the space discretization with a Cartesian rectangular mesh can be represented as a system of linear algebraic equations. The algebraic equations of this system for each internal grid point of the domain are called the stencil equations. For the 2D elasticity equations, two stencil equations can be written down for each grid point as follows:

$$\sum_{i=1}^{L} k_{j,i} u_i^{num} + \sum_{i=1}^{L} \bar{k}_{j,i} v_i^{num} = \bar{f}_j , \qquad j = 1, 2 , \qquad (6)$$

where u_i^{num} and v_i^{num} are the numerical solution for the displacements u and v at the ith grid point, $k_{j,i}$ and $\bar{k}_{j,i}$ are the unknown stencil coefficients corresponding to the displacements u and v (they should be determined), L is the number of the grid points included into a stencil, f_i are the components of the discretized body forces (see the next Sections). Many numerical techniques such as the finite difference method, the finite element method, the finite volume method, the isogeometric elements, the spectral elements, different meshless methods, and others can be finally reduced to Eq. (6) with some specific coefficients $k_{j,i}$ and $ar{k}_{i.i}$. In order to demonstrate a new technique, below we will assume compact 9-point stencils (L=9) in the 2D case that correspond to the width of the stencils for linear quadrilateral finite elements on Cartesian meshes and that require similar computational costs as those for linear finite elements. However, the stencils with any width can be used with the suggested approach.

Let us introduce the local truncation error used with OLTEM. The replacement of the numerical values of the displacements u_i^{num} and v_i^{num} at the grid points in Eq. (6) by the exact solution u_i and v_i to the elasticity equations, Eq. (1), leads to the residual of these equations called the local truncation error e_i of the discrete equations, Eq. (6):

$$e_j = \sum_{i=1}^{L} k_{j,i} u_i + \sum_{i=1}^{L} \bar{k}_{j,i} v_i - \bar{f}_j, \quad j = 1, 2.$$
 (7)

Calculating the difference between Eqs. (7) and (6), we can get

$$e_{j} = \sum_{i=1}^{L} \{k_{j,i} [u_{i} - u_{i}^{num}] + \bar{k}_{j,i} [v_{i} - v_{i}^{num}] \}$$

$$= \sum_{i=1}^{L} (k_{j,i} \bar{e}_{i} + \bar{k}_{j,i} \bar{e}_{i}^{*}) , \qquad j = 1, 2 , \qquad (8)$$

where $\bar{e}_i = u_i - u_i^{num}$ and $\bar{e}_i^* = v_i - v_i^{num}$ are the errors in the displacements u and v at the grid point i. As can be seen from Eq. (8), the local truncation errors e_i (i = 1, 2) are a linear combination of the errors in the displacements uand ν at the grid points which are included into the stencil equations.

In Section 2.1, OLTEM with 9-point compact stencils for the 2D elasticity equations is derived for heterogeneous materials with zero body forces. Its extension to nonzero body forces is considered in Section 2.2. 2D numerical

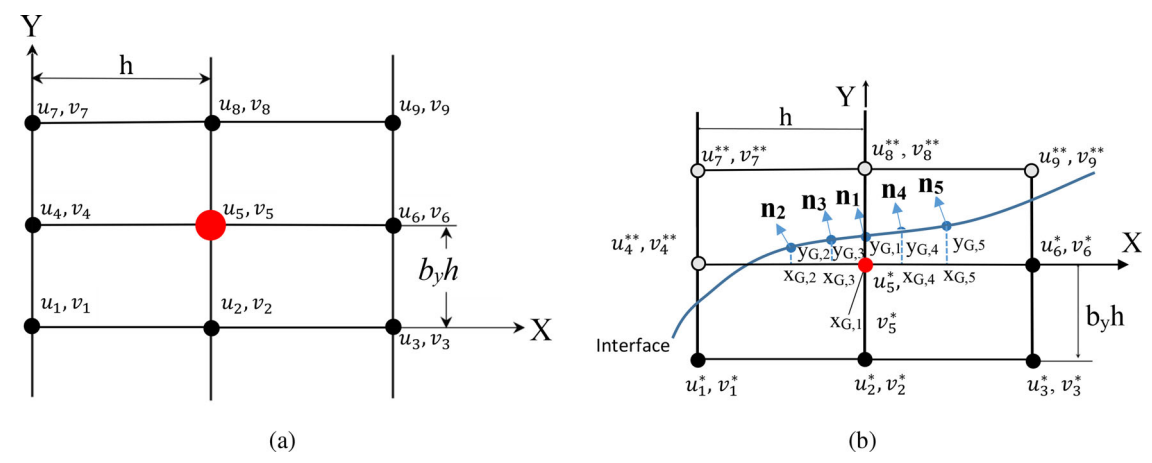


Figure 1. The spatial locations of the degrees of freedom u_p and v_p (p = 1, 2, ..., 9) that contribute to the 9-point uniform stencil for the internal degrees of freedom u_5 and v_5 for homogeneous material without interface (a) and for heterogeneous material with interface (b).

examples for elastic heterogeneous materials with an irregular interface and the different contrasts for Young's moduli as well as the comparison of OLTEM with FEM are presented in Section 3. For the derivation of many analytical expressions presented below, we use the computational program 'Mathematica'.

2. OLTEM for the 2D elasticity equations with discontinuous material properties

2.1. Zero body forces $f_x^l = 0$ and $f_y^l = 0$ in Eq. (1)

Let us consider a 2D bounded domain and a Cartesian rectangular mesh with a mesh size h where h is the size of the mesh along the x- axis, $b_y h$ is the size of the mesh along the y- axis (b_y is the aspect ratio of the mesh). To simplify derivations, below we consider regular rectangular domains with irregular interfaces between different materials. However, irregular domains can be also considered with OLTEM; see [39-41]. Here, we will develop 9-point uniform stencils that provide the second order of accuracy. We should mention that we use the same structure of stencils for homogeneous and heterogeneous materials (the difference between homogeneous and heterogeneous materials is in the values of the stencil coefficients only). The spatial locations of the 8 degrees of freedom that are close to the internal degree of freedom u_5 and contribute to the 9-point stencil for this degree of freedom are shown in Figure 1. For convenience, the local numeration of the grid points from 1 to 9 is used in Figure 1 as well as in the derivations below. The interface in Figure 1(b) divides the 9-point uniform stencil into two parts with different material properties. In order to impose the interface conditions at the interface, we select a small number of interface points as follows. First, we select one point at the interface with the coordinates $x_{G,1}$ and $y_{G,1}$. This point can be selected as the shortest distance from the internal grid point u_5 of the 9-point stencil to the interface. Then, we additionally select n interface points to the left and to the right from the point with the coordinates $x_{G,1}$ and $y_{G,1}$ at the same distances h = 0 $\sqrt{(x_{G,i+1}-x_{G,i})^2+(y_{G,i+1}-y_{G,i})^2}$ (i=1,2,...,2n) from each other; e.g., see Figure 1(b) for 9-point stencils. The numerical experiments show that small distances $\bar{h} = h/10$ yield accurate results. The total number of selected interface points is $N_G = 2n + 1$ where $N_G = 5$ is used for the 9-point stencils developed below.

Let us describe the coordinates of the grid points of the 9-point uniform stencils (see Figure 1) with respect to their central point (x_5, y_5) as follows:

$$x_p = x_5 + (i-2)h$$
, $y_p = y_5 + (j-2)b_yh$, (9)

for the 9-point stencils where p = 3(j - 1) + i with i, j = 1, 2, 3.

To describe the coordinates of the N_G points on the interface (see Figure 1(b)), we introduce $2N_G$ coefficients $d_{x,p}$ and $d_{y,p}$ ($p = 1, 2, ..., N_G$) as follows (see also Figure 1(b)):

$$x_{G,m} = x_G + d_{x,m}h, \quad y_{G,m} = y_G + d_{y,m}b_yh,$$

 $m = 1, 2, ..., N_G.$ (10)

Remark 2. Some of the interface points G_m $(m = 1, 2, ..., N_G)$ can be located slightly outside the 9-point cell. The derivations presented below are also valid for these cases.

The stencil equations, Eq. (6), for heterogeneous materials with the 9-point uniform stencil for the grid point (x_5, y_5) (see Figure 1) will be assumed in the following form:

$$\sum_{p=1}^{9} k_{j,p} \left[a_{p} u_{p}^{*,num} + (1 - a_{p}) u_{p}^{**,num} \right]$$

$$+ \sum_{p=1}^{9} \bar{k}_{j,p} \left[a_{p} v_{p}^{*,num} + (1 - a_{p}) v_{p}^{**,num} \right]$$

$$= \bar{f}_{i,5}, \qquad j = 1, 2,$$

$$(11)$$

where $\bar{f}_{j,5}=0$ in the case of zero body forces $f_x^l=f_y^l=0$ in Eq. (1), the unknown coefficients $k_{j,p}$ and $\bar{k}_{j,p}$ (p=1,2,...,9) are to be determined from the minimization of the local truncation error, the coefficients $a_p=1$ if the grid point u_p belongs to material * or $a_p=0$ if the grid point u_p belongs to another material ** (i.e., only two variables $u_p^{*,num}$, $v_p^{*,num}$ or $u_p^{**,num}$, $v_p^{**,num}$ are included into Eq.



(11) for each grid point; e.g., see Figure 1(b) with $a_1 = a_2 = a_3 = a_5 = a_6 = 1$ and $a_4 = a_7 = a_8 = a_9 = 0$).

Remark 3. Usually, stencil equations similar to Eq. (11) include the coefficient h^2 in the denominator in order to express the second space derivatives in the elasticity equations, Eq. (1). However, for convenience, the stencil equations, Eq. (11), are multiplied by h^2 in order to write down them without $\frac{1}{h^2}$. Therefore, the expressions for the local truncation error used in this article are also multiplied by h^2 .

The local truncation error e follows from Eq. (11) by the replacement of the numerical solution $u_p^{*,\,num},\,u_p^{**,\,num},\,v_p^{*,\,num}$ and $v_p^{**,\,num}$ by the exact solution $u_p^*,\,u_p^{**},\,v_p^*$ and v_p^{**} :

$$e_{j} = \sum_{p=1}^{9} k_{j,p} \left[a_{p} u_{p}^{*} + (1 - a_{p}) u_{p}^{**} \right]$$

$$+ \sum_{p=1}^{9} \bar{k}_{j,p} \left[a_{p} v_{p}^{*} + (1 - a_{p}) v_{p}^{**} \right] - \bar{f}_{j,5},$$

$$j = 1, 2.$$

$$(12)$$

One of the ideas of the new approach is to include the interface conditions for the exact solution at a small number of the interface points into Eq. (12) for the local truncation error as follows:

$$\begin{split} e_{j} &= \sum_{p=1}^{9} k_{j,p} \left[a_{p} u_{p}^{*} + (1 - a_{p}) u_{p}^{**} \right] + \sum_{p=1}^{9} \bar{k}_{j,p} \left[a_{p} v_{p}^{*} + (1 - a_{p}) v_{p}^{**} \right] \\ &+ \sum_{m=1}^{N_{G}} q_{1,m} (u_{G,m}^{*} - u_{G,m}^{**}) + \sum_{m=1}^{N_{G}} q_{2,m} (v_{G,m}^{*} - v_{G,m}^{**}) \\ &+ \sum_{m=1}^{N_{G}} h q_{3,m} \left\{ \left[n_{x,m} \left[(\dot{\lambda}_{*} + 2\mu_{*}) \frac{\partial u_{G,m}^{*}}{\partial x} + \dot{\lambda}_{*} \frac{\partial v_{G,m}^{*}}{\partial y} \right] + n_{y,m} \mu_{*} \left(\frac{\partial u_{G,m}^{*}}{\partial y} + \frac{\partial v_{G,m}^{*}}{\partial x} \right) \right] \right. \\ &- \left[n_{x,m} \left[(\dot{\lambda}_{**} + 2\mu_{**}) \frac{\partial u_{G,m}^{**}}{\partial x} + \dot{\lambda}_{**} \frac{\partial v_{G,m}^{**}}{\partial y} \right] + n_{y,m} \mu_{**} \left(\frac{\partial u_{G,m}^{*}}{\partial y} + \frac{\partial v_{G,m}^{*}}{\partial x} \right) \right] \right\} \\ &+ \sum_{m=1}^{N_{G}} h q_{4,m} \left\{ \left[n_{y,m} \left[(\dot{\lambda}_{*} + 2\mu_{*}) \frac{\partial v_{G,m}^{*}}{\partial y} + \dot{\lambda}_{*} \frac{\partial u_{G,m}^{*}}{\partial x} \right] + n_{x,m} \mu_{**} \left(\frac{\partial u_{G,m}^{*}}{\partial y} + \frac{\partial v_{G,m}^{*}}{\partial x} \right) \right] \right\} \\ &- \left[n_{y,m} \left[(\dot{\lambda}_{**} + 2\mu_{**}) \frac{\partial v_{G,m}^{*}}{\partial y} + \dot{\lambda}_{**} \frac{\partial u_{G,m}^{*}}{\partial x} \right] + n_{x,m} \mu_{**} \left(\frac{\partial u_{G,m}^{*}}{\partial y} + \frac{\partial v_{G,m}^{*}}{\partial x} \right) \right] \right\} - \bar{f}_{j,5}, \quad j = 1, 2, \end{split}$$

where $n_{x,m}$ and $n_{y,m}$ are the x and y-components of the normal vectors at the selected N_G interface points (e.g., see Figure 1(b)), the coefficients $q_{1,m}, q_{2,m}, q_{3,m}$, and $q_{4,m}$ ($m=1,2,...,N_G$) will be used for the minimization of the local truncation error in Eq. (13), the expressions in parenthesis after $q_{1,m}, q_{2,m}, q_{3,m}$, and $q_{4,m}$ are the interface conditions at the selected N_G interface points and are equal to zero (see Eqs. (3)–(5)). Therefore, Eqs. (12) and (13) yield the same local truncation error e_j . The addition of the interface conditions at $N_G = 5$ points in Eq. (13) with the coefficients $q_{1,m}, q_{2,m}, q_{3,m}$, and $q_{4,m}$ ($m=1,2,...,N_G$) allows us to get the second order of accuracy of OLTEM for general geometry of interfaces; see below.

Remark 4. In Eq. (13), we consider two local truncation errors for the first j=1 and second j=2 stencils. The coefficients $q_{1,m}$, $q_{2,m}$, $q_{3,m}$, and $q_{4,m}$ ($m=1,2,...,N_G$) are different for these two stencils. However, in order to simplify the

notations we omit index j for the coefficients $q_{1,m}$, $q_{2,m}$, $q_{3,m}$, and $q_{4,m}$.

Remark 5. Only $18+4N_G-1$ out of the $18+4N_G$ coefficients $k_{j,p}$, $\bar{k}_{j,p}$, $q_{1,m}$, $q_{2,m}$, $q_{3,m}$, $q_{4,m}$ (p=1,2,...,9, $m=1,2,...,N_G$) in Eq. (13) can be considered as unknown coefficients. This can be explained as follows. In the case of zero body forces $\bar{f}_{j,5}=0$, Eq. (13) can be rescaled by the division of the left- and right-hand sides of Eq. (13) by any scalar; i.e., one of the coefficients can be selected as unity and there will be only $18+4N_G-1$ unknown rescaled coefficients. The case of nonzero body forces $\bar{f}_{j,5}\neq 0$ can be similarly treated because the term $\bar{f}_{j,5}$ is a linear function of the stencil coefficients; see below. For convenience, we will scale the stencil coefficients in such a way that $k_{1,5}$ is $k_{1,5}=1$. Moreover, similar to finite element stencils we select $\bar{k}_{1,5}=0$.

In order to represent the local truncation error e_j as a Taylor series, let us expand the exact solution at the grid points and the selected N_G interface points in Eq. (13) into a Taylor series at small $h \ll 1$ in the vicinity of the central interface point G as follows:

$$c_{p} = c_{G} + \frac{\partial c_{G}}{\partial x} [((i-2) - dx_{G})h] + \frac{\partial c_{G}}{\partial y} [((l-2) - dy_{G})b_{y}h]$$

$$+ \frac{\partial^{2} c_{G}}{\partial x^{2}} \frac{[((i-2) - dx_{G})h]^{2}}{2!} + \frac{\partial^{2} c_{G}}{\partial y^{2}} \frac{[((l-2) - dy_{G})b_{y}h]^{2}}{2!}$$

$$+ 2 \frac{\partial^{2} c_{G}}{\partial x \partial y} \frac{[((i-2) - dx_{G})h][((l-2) - dy_{G})b_{y}h]}{2!}$$

$$+ ..., p = 3(l-1) + i \text{ with } i, l = 1, 2, 3$$
(14)

$$w_{j} = w_{G} + \frac{\partial w_{G}}{\partial x} \left[d_{x,j} h \right] + \frac{\partial w_{G}}{\partial y} \left[d_{y,j} b_{y} h \right] + \frac{\partial^{2} w_{G}}{\partial x^{2}} \frac{\left[d_{x,j} h \right]^{2}}{2!}$$

$$+ \frac{\partial^{2} w_{G}}{\partial y^{2}} \frac{\left[d_{y,j} b_{y} h \right]^{2}}{2!} + 2 \frac{\partial^{2} w_{G}}{\partial x \partial y} \frac{\left[(d_{x,j} h) \right] \left[d_{y,j} b_{y} h \right]}{2!} + \dots, \quad j = 1, 2, ..., 5$$

$$(15)$$

with $dx_G = \frac{x_G - x_5}{h}$ and $dy_G = \frac{y_G - y_5}{b_J h}$. In Eq. (14), the function c_p is u_p^* , u_p^{**} , v_p^* , v_p^{**} , v_p^{**} , in Eq. (15), the function w_j is $u_{G,j}^*$, $u_{G,j}^{**}$, $\frac{\partial u_{G,j}^*}{\partial x}$, $\frac{\partial u_{G,j}^{**}}{\partial x}$, $\frac{\partial u_{G,j}^{**}}{\partial y}$, $\frac{\partial u_{G,j}^{**}}{\partial y}$, $v_{G,j}^{**}$, $v_{G,j}^{**}$, $\frac{\partial v_{G,j}^{**}}{\partial x}$, $\frac{\partial v_{G,j}^{**}}{\partial x}$, $\frac{\partial v_{G,j}^{**}}{\partial y}$, $\frac{\partial v_{G,j}^{**}}{\partial y}$. The exact solution u_G^* , u_G^{**} , v_G^* and v_G^{**} to the elasticity equations, Eq. (1), at the central interface point with the coordinates $x = x_G$ and $y = y_G$ meets the following equations:

$$\frac{\partial^{2} u_{G}^{*}}{\partial x^{2}} = -\left[\frac{\mu_{*}}{(2\mu_{*} + \lambda_{*})} \frac{\partial^{2} u_{G}^{*}}{\partial y^{2}} + \frac{(\mu_{*} + \lambda_{*})}{(2\mu_{*} + \lambda_{*})} \frac{\partial^{2} v_{G}^{*}}{\partial x \partial y} + \frac{1}{(2\mu_{*} + \lambda_{*})} f_{G,x}^{*}\right],$$
(16)

$$\frac{\partial^2 v_G^*}{\partial x^2} = -\left[\frac{(2\mu_* + \lambda_*)}{\mu_*} \frac{\partial^2 v_G^*}{\partial y^2} + \frac{(\mu_* + \lambda_*)}{\mu_*} \frac{\partial^2 u_G^*}{\partial x \partial y} + \frac{1}{\mu_*} f_{G,y}^*\right],$$
(17)

$$\frac{\partial^2 u_G^{**}}{\partial x^2} = -\left[\frac{\mu_{**}}{(2\mu_{**} + \lambda_{**})} \frac{\partial^2 u_G^{**}}{\partial y^2} + \frac{(\mu_{**} + \lambda_{**})}{(2\mu_{**} + \lambda_{**})} \frac{\partial^2 v_G^{**}}{\partial x \partial y} + \frac{1}{(2\mu_{**} + \lambda_{**})} f_{G,x}^{**}\right],$$
(18)

$$\frac{\partial^2 v_G^{**}}{\partial x^2} = -\left[\frac{(2\mu_{**} + \lambda_{**})}{\mu_{**}} \frac{\partial^2 v_G^{**}}{\partial y^2} + \frac{(\mu_{**} + \lambda_{**})}{\mu_{**}} \frac{\partial^2 u_G^{**}}{\partial x \partial y} + \frac{1}{\mu_{**}} f_{G,y}^{**} \right] , \tag{19}$$

$$\frac{\partial^{(2+i+j)} u_G^*}{\partial x^{(2+i)} \partial y^j} = -\left[\frac{\mu_*}{(2\mu_* + \lambda_*)} \frac{\partial^{(2+i+j)} u_G^*}{\partial x^i \partial y^{(2+j)}} + \frac{(\mu + \lambda)}{(2\mu_* + \lambda_*)} \frac{\partial^{(2+i+j)} v_G^*}{\partial x^{(i+1)} \partial y^{(j+1)}} + \frac{1}{(2\mu_* + \lambda_*)} \frac{\partial^{(i+j)} f_{G,x}^*}{\partial x^i \partial y^j} \right], \tag{20}$$

$$\frac{\partial^{(2+i+j)}v_{G}^{*}}{\partial x^{(2+i)}\partial y^{j}} = -\left[\frac{(2\mu_{*} + \lambda_{*})}{\mu_{*}}\frac{\partial^{(2+i+j)}v_{G}^{*}}{\partial x^{i}\partial y^{(2+j)}} + \frac{(\mu_{*} + \lambda_{*})}{\mu_{*}}\frac{\partial^{(2+i+j)}u_{G}^{*}}{\partial x^{(i+1)}\partial y^{(j+1)}} + \frac{1}{\mu_{*}}\frac{\partial^{(i+j)}f_{G,y}^{*}}{\partial x^{i}\partial y^{j}}\right],$$
(21)

$$\frac{\partial^{(2+i+j)} u_G^{**}}{\partial x^{(2+i)} \partial y^j} = -\left[\frac{\mu_{**}}{(2\mu_{**} + \lambda_{**})} \frac{\partial^{(2+i+j)} u_G^{**}}{\partial x^i \partial y^{(2+j)}} + \frac{(\mu + \lambda)}{(2\mu_{**} + \lambda_{**})} \frac{\partial^{(2+i+j)} v_G^{**}}{\partial x^{(i+1)} \partial y^{(j+1)}} + \frac{1}{(2\mu_{**} + \lambda_{**})} \frac{\partial^{(i+j)} f_{G,x}^{**}}{\partial x^i \partial y^j} \right], \tag{22}$$

$$\frac{\partial^{(2+i+j)}v_G^{**}}{\partial x^{(2+i)}\partial y^j} = -\left[\frac{(2\mu_{**} + \lambda_{**})}{\mu_{**}}\frac{\partial^{(2+i+j)}v_G^{**}}{\partial x^i\partial y^{(2+j)}} + \frac{(\mu_{**} + \lambda_{**})}{\mu_{**}}\frac{\partial^{(2+i+j)}u_G^{**}}{\partial x^{(i+1)}\partial y^{(j+1)}} + \frac{1}{\mu_{**}}\frac{\partial^{(i+j)}f_{G,y}^{**}}{\partial x^i\partial y^j}\right],$$
(23)

with $i, j = 0, 1, 2, 3, 4, \dots$ We should mention that Eqs. (16)–(19) directly follow from Eq. (1) while Eqs. (20)–(23) are obtained by the differentiation of Eqs. (16)–(19) with respect to x and y.

Remark 6. In Eqs. (16)–(19), we have expressed the second x derivatives in terms of the second y derivatives and the second mixed derivatives. However, similarly we can express the second y derivatives in terms of the second x derivatives and the second mixed derivatives. This latter case (with the corresponding modifications of Eqs. (20)–(23) will be used for the calculation of the local truncation error and the stencil coefficients for the second stencil equation with j=2; see below.

Remark 7. It is interesting to mention that for anisotropic materials, each elasticity equation, Eq. (1), will include the all partial derivatives $\frac{\partial^2}{\partial x^2}$, $\frac{\partial^2}{\partial y^2}$, and $\frac{\partial^2}{\partial x \partial y}$ of the displacements u and v. Then, by the summation and the deduction of these two equations multiplied by some coefficients, the term $\frac{\partial^2 v}{\partial x^2}$ can be excluded from the first elasticity equation and the term $\frac{\partial^2 u}{\partial x^2}$ can be excluded from the second elasticity equation; i.e., Eqs. (16) and (17) for anisotropic case can be similarly written with some additional derivatives $\frac{\partial^2}{\partial y^2}$ and $\frac{\partial^2}{\partial x \partial y}$ of the displacements u and v in the right-hand side of Eqs. (16) and (17). For anisotropic materials the interface conditions, Eq. (5) includes the same partial derivatives of the displacements u and v with different elastic constants. The extension of OLTEM to anisotropic materials will be considered in detail in the future.

Below, we consider the local truncation error for the first stencil equation, Eq. (13) with j=1. The derivations of the local truncation error for the second stencil equation, Eq. (13) with j=2, can be done similarly (see also Remark 6). Inserting Eqs. (14) and (15) and Eqs. (16)–(23) with zero body forces $f_{G,x}^* = f_{G,y}^{**} = f_{G,x}^{**} = f_{G,y}^{**} = 0$ into Eq. (13), we will get the following local truncation error in space e_1 :

$$\begin{split} e_{1} &= b_{1,1}u_{G}^{*} + b_{1,2}v_{G}^{*} + b_{1,3}u_{G}^{***} + b_{1,4}v_{G}^{***} + h\left(b_{1,5}\frac{\partial u_{G}^{*}}{\partial x} + b_{1,6}\frac{\partial v_{G}^{*}}{\partial x} + b_{1,7}\frac{\partial u_{G}^{**}}{\partial x} + b_{1,9}\frac{\partial u_{G}^{*}}{\partial x} + b_{1,19}\frac{\partial v_{G}^{*}}{\partial y} + b_{1,11}\frac{\partial u_{G}^{**}}{\partial y} + b_{1,12}\frac{\partial v_{G}^{**}}{\partial y}\right) \\ &+ h^{2}\left(b_{1,13}\frac{\partial^{2}u_{G}^{*}}{\partial x\partial y} + b_{1,14}\frac{\partial^{2}v_{G}^{*}}{\partial x\partial y} + b_{1,15}\frac{\partial^{2}u_{G}^{**}}{\partial x\partial y} + b_{1,16}\frac{\partial^{2}v_{G}^{**}}{\partial x\partial y} + b_{1,17}\frac{\partial^{2}u_{G}^{*}}{\partial y^{2}} + b_{1,18}\frac{\partial^{2}v_{G}^{*}}{\partial y^{2}} + b_{1,19}\frac{\partial^{2}u_{G}^{**}}{\partial y^{2}} + b_{1,20}\frac{\partial^{2}v_{G}^{**}}{\partial y^{2}}\right) \\ &+ h^{3}\left(b_{1,21}\frac{\partial^{3}u_{G}^{*}}{\partial x\partial y^{2}} + b_{1,22}\frac{\partial^{3}v_{G}^{**}}{\partial x\partial y^{2}} + b_{1,23}\frac{\partial^{3}v_{G}^{**}}{\partial x\partial y^{2}} + b_{1,24}\frac{\partial^{3}v_{G}^{**}}{\partial x\partial y^{3}} + b_{1,25}\frac{\partial^{3}u_{G}^{*}}{\partial y^{3}} + b_{1,27}\frac{\partial^{3}u_{G}^{*}}{\partial y^{3}} + b_{1,28}\frac{\partial^{3}v_{G}^{**}}{\partial y^{3}}\right) \\ &+ h^{4}\left(b_{1,29}\frac{\partial^{4}u_{G}^{*}}{\partial x\partial y^{3}} + b_{1,30}\frac{\partial^{4}v_{G}^{**}}{\partial x\partial y^{3}} + b_{1,31}\frac{\partial^{4}u_{G}^{**}}{\partial x\partial y^{3}} + b_{1,32}\frac{\partial^{4}v_{G}^{**}}{\partial x\partial y^{3}} + b_{1,33}\frac{\partial^{4}u_{G}^{*}}{\partial y^{4}} + b_{1,35}\frac{\partial^{4}u_{G}^{*}}{\partial y^{4}} + b_{1,35}\frac{\partial^{4}u_{G}^{**}}{\partial y^{4}} + b_{1,36}\frac{\partial^{5}v_{G}^{**}}{\partial y^{5}}\right) \\ &+ h^{5}\left(b_{1,37}\frac{\partial^{5}u_{G}^{*}}{\partial x\partial y^{4}} + b_{1,38}\frac{\partial^{5}v_{G}^{*}}{\partial x\partial y^{4}} + b_{1,40}\frac{\partial^{5}v_{G}^{**}}{\partial x\partial y^{4}} + b_{1,41}\frac{\partial^{5}u_{G}^{*}}{\partial y^{5}} + b_{1,42}\frac{\partial^{5}v_{G}^{*}}{\partial y^{5}} + b_{1,44}\frac{\partial^{5}v_{G}^{*}}{\partial y^{5}}\right) \\ &+ h^{6}\left(b_{1,45}\frac{\partial^{6}u_{G}^{*}}{\partial x\partial y^{5}} + b_{1,47}\frac{\partial^{6}u_{G}^{*}}{\partial x\partial y^{5}} + b_{1,48}\frac{\partial^{6}v_{G}^{*}}{\partial x\partial y^{5}} + b_{1,49}\frac{\partial^{6}u_{G}^{*}}{\partial y^{6}} + b_{1,51}\frac{\partial^{6}u_{G}^{*}}{\partial y^{6}} + b_{1,51}\frac{\partial^{6}v_{G}^{*}}{\partial y^{6}} + b_{1,51}\frac{\partial^{6}v_{G}^{*}}{\partial y^{6}} + b_{1,52}\frac{\partial^{6}v_{G}^{*}}{\partial y^{6}} + b$$

where the coefficients $b_{1,p}$ (p = 1, 2, ...) are expressed in terms of the coefficients $k_{1,i}$, $k_{1,i}$ and $q_{1,m}$, $q_{2,m}$, $q_{3,m}$, $q_{4,m}$ (i = 1, 2, ..., 9, $m = 1, 2, ..., N_G$) and are given in Appendix A. Here, we should mention that the expression for the local truncation error e_1 , Eq. (24), includes only the first-order derivatives with respect to x (the higher-order derivatives with respect to x are excluded with the help of Eqs. (16)–(23)).



2.1.1. Homogeneous materials (no interface)

For homogeneous materials all a_i (j = 1, 2, ..., 9) coefficients are $a_i = 1$ (see Eq. (11) if we consider material *) as well as all $q_{1,j} = q_{2,j} = q_{3,j} = q_{4,j} = 0$ (j = 1, 2, ..., 5) coefficients are zero. In this case, the derivation of the local truncation error is similar to that in the previous section and is given in our article [35]. The corresponding stencils coefficients can be analytically found and they are (for convenience, the matrix form is used below for the representation of these coefficients):

application of OLTEM to the Poisson equation for which at the same 9-point stencils the accuracy was improved by two orders for rectangular meshes and by four orders for square meshes compared to linear finite elements; see [42].

2.1.2. 9-Point stencils for heterogeneous materials with an irregular interface

The formulas presented below can be used for the first j=1and second j=2 stencils (they should be separately consid-

$$\frac{\begin{pmatrix} k_{1,7} & k_{1,8} & k_{1,9} \\ k_{1,4} & k_{1,5} & k_{1,6} \\ k_{1,1} & k_{1,2} & k_{1,3} \end{pmatrix}}{k_{1,4} & k_{1,5} & k_{1,6} \\ k_{2,1} & \bar{k}_{2,2} & \bar{k}_{2,3} \end{pmatrix}^{T}} = \begin{pmatrix} \bar{k}_{2,7} & \bar{k}_{2,8} & \bar{k}_{2,9} \\ \bar{k}_{2,4} & \bar{k}_{2,5} & \bar{k}_{2,6} \\ \bar{k}_{2,1} & \bar{k}_{2,2} & \bar{k}_{2,3} \end{pmatrix}^{T} \\
= \begin{pmatrix} -\lambda b_{y}^{2} - 2\mu b_{y}^{2} + \lambda + \mu \\ 4(2\lambda b_{y}^{2} + \lambda + 4(b_{y}^{2} + 1)\mu) & \frac{(b_{y}^{2} - 1)\lambda + 2(b_{y}^{2} - 2)\mu}{2(2eb_{y}^{2} + \lambda + 4(b_{y}^{2} + 1)\mu)} & \frac{-\lambda b_{y}^{2} - 2\mu b_{y}^{2} + \lambda + \mu}{4(2\lambda b_{y}^{2} + \lambda + \mu)} \\
- \frac{2\lambda b_{y}^{2} + 4\mu b_{y}^{2} + \lambda + \mu}{2(2\lambda b_{y}^{2} + \lambda + 4(b_{y}^{2} + 1)\mu)} & 1 & -\frac{2\lambda b_{y}^{2} + 4\mu b_{y}^{2} + \lambda + \mu}{2(2\lambda b_{y}^{2} + \lambda + 4(b_{y}^{2} + 1)\mu)} \\
- \frac{-\lambda b_{y}^{2} - 2\mu b_{y}^{2} + \lambda + \mu}{4(2\lambda b_{y}^{2} + \lambda + \mu)} & \frac{(b_{y}^{2} - 1)\lambda + 2(b_{y}^{2} - 2)\mu}{2(2\lambda b_{y}^{2} + \lambda + 4(b_{y}^{2} + 1)\mu)} & \frac{-\lambda b_{y}^{2} - 2\mu b_{y}^{2} + \lambda + \mu}{4(2\lambda b_{y}^{2} + \lambda + \mu)} \\
- \frac{k_{1,7}}{4(2\lambda b_{y}^{2} + \lambda + 4(b_{y}^{2} + 1)\mu)} & \frac{(b_{y}^{2} - 1)\lambda + 2(b_{y}^{2} - 2)\mu}{2(2\lambda b_{y}^{2} + \lambda + 4(b_{y}^{2} + 1)\mu)} & \frac{-\lambda b_{y}^{2} - 2\mu b_{y}^{2} + \lambda + \mu}{4(2\lambda b_{y}^{2} + \lambda + \mu)} \\
- \frac{k_{1,7}}{4(2\lambda b_{y}^{2} + \lambda + 4(b_{y}^{2} + 1)\mu)} & \frac{(b_{y}^{2} - 1)\lambda + 2(b_{y}^{2} - 2)\mu}{2(2\lambda b_{y}^{2} + \lambda + 4(b_{y}^{2} + 1)\mu)} & \frac{-\lambda b_{y}^{2} - 2\mu b_{y}^{2} + \lambda + \mu}{4(2\lambda b_{y}^{2} + \lambda + \mu)} \\
- \frac{k_{1,7}}{4(2\lambda b_{y}^{2} + \lambda + 4(b_{y}^{2} + 1)\mu)} & \frac{(b_{y}^{2} - 1)\lambda + 2(b_{y}^{2} - 2)\mu}{2(2\lambda b_{y}^{2} + \lambda + 4(b_{y}^{2} + 1)\mu)} & \frac{-\lambda b_{y}^{2} - 2\mu b_{y}^{2} + \lambda + \mu}{4(2\lambda b_{y}^{2} + \lambda + \mu)} \\
- \frac{k_{1,7}}{4(2\lambda b_{y}^{2} + \lambda + 4(b_{y}^{2} + 1)\mu)} & 0 & -\frac{3b_{y}(\lambda + \mu)}{8(2\lambda b_{y}^{2} + \lambda + 4(b_{y}^{2} + 1)\mu)} \\
- \frac{k_{1,7}}{4(2\lambda b_{y}^{2} + \lambda + 4(b_{y}^{2} + 1)\mu)} & 0 & -\frac{3b_{y}(\lambda + \mu)}{8(2\lambda b_{y}^{2} + \lambda + 4(b_{y}^{2} + 1)\mu)} \\
- \frac{k_{1,7}}{4(2\lambda b_{y}^{2} + \lambda + 4(b_{y}^{2} + 1)\mu)} & 0 & -\frac{3b_{y}(\lambda + \mu)}{8(2\lambda b_{y}^{2} + \lambda + 4(b_{y}^{2} + 1)\mu)} \\
- \frac{k_{1,7}}{4(2\lambda b_{y}^{2} + \lambda + 4(b_{y}^{2} + 1)\mu)} & 0 & -\frac{3b_{y}(\lambda + \mu)}{8(2\lambda b_{y}^{2} + \lambda + 4(b_{y}^{2} + 1)\mu)} \\
- \frac{k_{1,7}}{4(2\lambda b_{y}^{2} + \lambda$$

with the following local truncation error for the first stencil (see our article [35] for details):

$$e_{1} = \frac{b_{y}^{2}((b_{y}^{2} - 2)\mu - \lambda)}{8(2b_{y}^{2}\lambda + 4(b_{y}^{2} + 1)\mu + \lambda)} \frac{\partial^{4}u_{G}^{*}}{\partial y^{4}}h^{4} + O(h^{5}),$$
 (26)

i.e., the order of the local truncation error cannot exceed four for any 9-point uniform stencils independent of the method used for their derivation (the finite element method, the finite volume method, the finite difference method, or any other method). The fourth order of the local truncation error corresponds to the second order of accuracy for the global numerical solution (e.g., see our article [35]) and is the same as that for linear finite elements. These results are different from the ered for j = 1 and j = 2). In order to minimize the order of the local truncation error e_1 in Eq. (24), we will zero the first 20 coefficients $b_{j,p}$ in Eq. (24) up to the second order with respect to *h*; i.e.,

$$b_{i,p} = 0, p = 1, 2, ..., 20.$$
 (27)

Then, in order to have a sufficient number of equations for the calculation of the 38 stencil coefficients of each stencil including $k_{i,i}$, $k_{i,i}$ (i = 1, 2, ..., 9) and $q_{1,m}$, $q_{2,m}$, $q_{3,m}$, $q_{4,m}$ (m = 1, 2, ..., 5), we use the least square method for the minimization of coefficients $b_{j,p}$ related to the third, fourth, fifth, and sixth orders of the local truncation error with the following residual R_i :

$$R_{j} = \sum_{p=21}^{28} b_{j,p}^{2} + h_{1} \sum_{p=29}^{36} b_{j,p}^{2} + h_{2} \sum_{p=37}^{44} b_{j,p}^{2} + h_{3} \sum_{p=45}^{52} b_{j,p}^{2},$$
(28)

where h_1 , h_2 , and h_3 are the weighting factors to be selected (e.g., the numerical experiments show that $h_1 = h_2 = h_3 = 0.1$ yield accurate results). In order to minimize the residual R_j with the constraints given by Eq. (27), we can form a new residual \overline{R}_j with the Lagrange multipliers λ_i :

$$\bar{R}_{j} = \sum_{l=1}^{20} \lambda_{l} b_{j,l} + \sum_{p=21}^{28} b_{j,p}^{2} + h_{1} \sum_{p=29}^{36} b_{j,p}^{2} + h_{2} \sum_{p=37}^{44} b_{j,p}^{2} + h_{3} \sum_{p=45}^{52} b_{j,p}^{2}.$$

$$(29)$$

The residual \bar{R}_j is a quadratic function of the stencil coefficients $k_{j,i}$, $\bar{k}_{j,i}$ (i=1,2,...,9) and $q_{1,m}$, $q_{2,m}$, $q_{3,m}$, $q_{4,m}$ (m=1,2,...,5) and a linear function of the Lagrange multipliers λ_l ; i.e., $\bar{R}_j = \bar{R}_j(k_{j,i},\bar{k}_{j,i},q_{1,m},q_{2,m},q_{3,m},q_{4,m},\lambda_l)$. In order to minimize the residual $\bar{R}_j = \bar{R}_j(k_{j,i},\bar{k}_{j,i},q_{1,m},q_{2,m},q_{3,m},q_{4,m},\lambda_l)$, the following equations based on the least square method for the residual \bar{R}_j can be written down:

$$\frac{\partial \bar{R}_{j}}{\partial k_{j,i}} = 0, \quad \frac{\partial \bar{R}_{j}}{\partial \bar{k}_{j,i}} = 0, \quad \frac{\partial \bar{R}_{j}}{\partial q_{1,m}} = 0, \quad \frac{\partial \bar{R}_{j}}{\partial q_{2,m}} = 0,$$

$$\frac{\partial \bar{R}_{j}}{\partial q_{3,m}} = 0, \quad \frac{\partial \bar{R}_{j}}{\partial q_{4,m}} = 0, \quad \frac{\partial \bar{R}_{j}}{\partial \lambda_{l}} = 0,$$

$$i = 1, 2, ..., 9, \quad m = 1, 2, ..., 5, \quad l = 1, 2, ..., 20,$$
(30)

where equations $\frac{\partial \overline{R}_1}{\partial k_{1,5}} = \frac{\partial \overline{R}_1}{\partial k_{1,5}} = 0$ should be replaced by $k_{1,5}=1$ and $\bar{k}_{1,5}=0$ for the first stencil with j=1 $(\frac{\partial \overline{R}_2}{\partial k_{2,5}} = \frac{\partial \overline{R}_2}{\partial \bar{k}_{2,5}} = 0$ should be replaced by $k_{2,5} = 0$ and $\bar{k}_{2,5} = 0$ 1 for the second stencil with j = 2); see Remark 5. Eq. (30) forms a system of 58 linear algebraic equations with respect to 58 unknown coefficients $k_{j,i}$, $\bar{k}_{j,i}$ (i = 1, 2, ..., 9) and $q_{1,m}, q_{2,m}, q_{3,m}, q_{4,m}$ (m = 1, 2, ..., 5) as well as 20 Lagrange multipliers λ_l (l = 1, 2, ..., 20). Solving these linear algebraic equations numerically, we can find the coefficients $k_{i,i}$, $\bar{k}_{i,i}$ (i = 1, 2, ..., 9) for the 9-point uniform stencils as well as $q_{1,m}, q_{2,m}, q_{3,m}, q_{4,m}$ (m = 1, 2, ..., 5). As can be seen, the presented procedure provides the third order of the local truncation error for the 9-point uniform stencils with the general geometry of the interface. The 9-point uniform stencils of OLTEM for homogeneous materials (without interface) provide the fourth order of the local truncation error for rectangular meshes; see Eq. (26). This leads to the second order of accuracy of global solutions; see the numerical examples below. Moreover, due to the minimization of the leading high-order terms $b_{j,p}$ of the local

truncation error with Eq. (29), at the same numbers of degrees of freedom and the engineering accuracy, OLTEM with irregular interfaces yields more accurate results than those obtained by high-order finite elements (up to the third order) with much wider stencils; see the numerical examples below.

Remark 8. To estimate the computational costs for the solution of 58 linear algebraic equations formed by Eq. (30) for the 9-point stencils, we solved 10⁶ such systems with the general MATLAB solver on a desktop computer (Processor: Intel (R) Core(TN) i9-9900 CPU @3.10Hz 3.10 HZ). The computation 'wall' time was T = 7649.19s for 10^6 systems or the average time for one system was 0.007649s for the 9-point stencils. Because the coefficients $k_{i,i}$, $\bar{k}_{i,i}$ are independently calculated for different grid points, the computation time of their calculation for different grid points can be significantly reduced on modern parallel computers. This means that for large global systems of discrete equations, the computation time for the calculation of the coefficients $k_{i,i}$, $k_{i,i}$ is very small compared to that for the solution of the global system of discrete equations. We should mention that the coefficients $q_{1,m}$, $q_{2,m}$, $q_{3,m}$, $q_{4,m}$ calculated from the local system of equations, Eq. (30), are only used for the calculation of non-zero right-hand side vector while the Lagrange multipliers λ_l in the local system of equations, Eq. (30), are not used in the global system of discrete equations at all.

Remark 9. It is interesting to mention that the stencil coefficients can be also derived by using the central grid point with the coordinates x_5 and y_5 in Eqs. (14)–(24) instead of the interface point with the coordinates x_G and y_G .

The global system of discrete equations includes the 9-point stencils for homogeneous materials without interfaces and the 9-point stencils for heterogeneous materials with interfaces between different materials (see Figure 1) for all internal grid points located inside the domain. OLTEM does not use unknowns at the interfaces and the global system of discrete equations has the same unknowns $k_{j,p}$, $\bar{k}_{j,p}$ (see Eq. (11)) for homogeneous and heterogeneous materials (the same structures of the global matrices, the difference are only in the values of the stencil coefficients $k_{j,i}$, $\bar{k}_{j,i}$ of the global matrices).

2.2. Nonzero body forces $\mathbf{f}_{\mathbf{x}}^{l} \neq \mathbf{0}$ and $\mathbf{f}_{\mathbf{y}}^{l} \neq \mathbf{0}$ in Eq. (1)

The inclusion of non-zero body forces $f_x^l \neq 0$ and $f_y^l \neq 0$ in the PDEs, Eq. (1), leads to the non-zero terms $\bar{f}_{j,5}$ in the stencil equations, Eq. (11) (similar to Eq. (6)). As we mentioned after Eq. (1), the body forces f_x^l and f_y^l can be discontinuous across the interfaces. The expressions for the terms $\bar{f}_{j,5}$ can be calculated from the procedure used for the derivation of the local truncation error in the case of zero body forces as follows (here, we will show the derivation of the term $\bar{f}_{1,5}$ for the first stencil equation, Eq. (11), with j=1.) The insertion of Eqs. (14) and (15) and Eqs. (16)–(23) with non-zero body forces into Eq. (13) yields the following local truncation error in space e_1^f :

$$\begin{split} e_1^f &= e_1 - [\bar{f}_{1,5} + \mathbf{h}^2 (\frac{1}{2\lambda_* + 4\mu_*} ((q_1d_{x_1}^2 + 2\lambda_* n_{y,1}q_16d_{x,1} + 2\lambda_* n_{x,1}q_6d_{x,1} + 4n_{x,1}\lambda_* q_6d_{x,1} + a_1k_1 + a_3k_3 + a_4k_4 + a_6k_6 \\ &+ a_7k_7 + a_9k_9 + 2d_{x,5}\lambda_* n_{x,5}q_{10} + 4d_{x,5}n_{x,5}\mu_* q_{10} + 2d_{x,2}\lambda_* n_{y,2}q_{17} + 2d_{x,3}\lambda_* n_{y,3}q_{18} + 2d_{x,4}\lambda_* n_{y,4}q_{19} + d_{x,2}^2 q_2 + 2d_{x,5}\lambda_* n_{y,5}q_{20} + d_{x,3}^2 q_3 \\ &+ d_{x,4}^2q_4 + d_{x,5}^2q_5 + 2d_{x,2}\lambda_* n_{x,2}q_7 + 4d_{x,2}n_{x,2}\mu_* q_7 + 2d_{x,3}\lambda_* n_{x,3}q_8 + 4d_{x,3}n_{x,3}\mu_* q_8 + 2d_{x,4}\lambda_* n_{x,4}q_9 + 4d_{x,4}n_{x,4}\mu_* q_9)(f_{G,x}^*)) \\ &- \frac{1}{2\mu_*} ((q_11d_{x,1}^2 + 2n_{x,1}\lambda_* q_16d_{x,1} + 2n_{y,1}\lambda_* q_6d_{x,1} + a_1\bar{k}_1 + a_3\bar{k}_3 + a_4\bar{k}_4 + a_6\bar{k}_6 + a_7\bar{k}_7 + a_9\bar{k}_9 \\ &+ 2d_{x,5}n_{y,5}\mu_* q_{10} + d_{x,2}^2q_{12} + d_{x,3}^2q_{13} + d_{x,4}^2q_{14} + d_{x,5}^2q_{15} + 2d_{x,2}n_{x,2}\mu_* q_{17} \\ &+ 2d_{x,3}n_{x,3}\mu_* q_{18} + 2d_{x,4}n_{x,4}\mu_* q_{19} + 2d_{x,5}n_{x,5}\mu_* q_{20} + 2d_{x,2}n_{y,2}\mu_* q_7 + 2d_{x,3}n_{y,3}\mu_* q_8 + 2d_{x,4}n_{y,4}\mu_* q_9)(f_{G,y}^*)) \\ &+ \frac{1}{2(\lambda_* + 2\mu_*)} ((q_1d_{x,1}^2 + 2\lambda_{**}n_{y,1}q_16d_{x,1} + 2\lambda_{**}n_{x,1}q_6d_{x,1} + 4n_{x,1}\mu_{**}q_6d_{x,1} + (a_1 - 1)k_1 + (a_3 - 1)k_3 \\ &+ a_4k_4 - k_4 + a_6k_6 - k_6 + a_7k_7 - k_7 + a_9k_9 \\ &- k_9 + 2d_{x,5}\lambda_* n_{x,5}q_{10} + 4d_{x,5}n_{x,5}\mu_* q_{10} + 2d_{x,2}\lambda_* n_{y,2}q_{17} + 2d_{x,3}\lambda_* n_{y,3}q_{18} + 2d_{x,4}\lambda_* n_{y,4}q_{19} + d_{x,2}^2q_2 \\ &+ 2d_{x,5}\lambda_* n_{x,5}q_{20} + d_{x,3}^2q_3 + d_{x,4}^2q_4 + d_{x,5}^2q_5 \\ &+ 2d_{x,2}\lambda_* n_{x,2}q_7 + 4d_{x,2}n_{x,2}\mu_* + q_7 + 2d_{x,3}\lambda_* n_{x,3}q_8 + 4d_{x,3}n_{x,3}\mu_* q_8 + 2d_{x,4}\lambda_* n_{x,4}q_9 + 4d_{x,4}n_{x,4}\mu_* q_9)(f_{G,x}^{**})) \\ &+ \frac{1}{2\mu_*} ((q_11d_{x,1}^2 + 2n_{x,1}\mu_* q_16d_{x,1} + 2n_{y,1}\mu_* q_6d_{x,1} + (a_1 - 1)\bar{k}_1 + (a_3 - 1)\bar{k}_3 + a_4\bar{k}_4 - \bar{k}_4 \\ &+ a_6\bar{k}_6 - \bar{k}_6 + a_7\bar{k}_7 - \bar{k}_7 + a_9\bar{k}_9 - \bar{k}_9 + 2d_{x,5}n_{y,5}\mu_* q_{10} \\ &+ d_{x,2}^2q_{12} + d_{x,3}^2q_{13} + d_{x,4}^2q_{14} + d_{x,5}^2q_{15} + 2d_{x,2}n_{x,2}\mu_* q_{17} + 2d_{x,3}n_{x,3}\mu_* q_{1$$

where e_1 is the local truncation error in space given by Eq. (24) for zero body forces, $\tilde{f}_{G,x}^*$, $\tilde{f}_{G,y}^{**}$, and $\tilde{f}_{G,y}^{**}$ designate the body forces f_x^* , f_x^{**} , f_y^* and f_y^{**} calculated at the central interface point with the coordinates $x = x_G$ and $y = y_G$. Equating to zero the expression in the square brackets in the right-hand side of Eq. (31), we will get the expression for $\bar{f}_{1,5}$:

$$\begin{split} \bar{f}_{1,5} &= -\mathbf{h}^2 (\frac{1}{2\lambda_* + 4\mu_*} ((q_1d_{x,1}^2 + 2\lambda_* n_{y,1}q_{16}d_{x,1} + 2\lambda_* n_{x,1}q_6d_{x,1} + 4n_{x,1}\lambda_* q_6d_{x,1} + a_1k_1 + a_3k_3 + a_4k_4 + a_6k_6 \\ &+ a_7k_7 + a_9k_9 + 2d_{x,5}\lambda_* n_{x,5}q_{10} + 4d_{x,5}n_{x,5}\mu_* q_{10} + 2d_{x,2}\lambda_* n_{y,2}q_{17} + 2d_{x,3}\lambda_* n_{y,3}q_{18} + 2d_{x,4}\lambda_* n_{y,4}q_{19} + d_{x,2}^2q_2 + 2d_{x,5}\lambda_* n_{y,5}q_{20} + d_{x,3}^2q_3 \\ &+ d_{x,4}^2q_4 + d_{x,5}^2q_5 + 2d_{x,2}\lambda_* n_{x,2}q_7 + 4d_{x,2}n_{x,2}\mu_* q_7 + 2d_{x,3}\lambda_* n_{x,3}q_8 + 4d_{x,3}n_{x,3}\mu_* q_8 + 2d_{x,4}\lambda_* n_{x,4}q_9 + 4d_{x,4}n_{x,4}\mu_* q_9)(f_{G,x}^2)) \\ &- \frac{1}{2\mu_*} ((q_{11}d_{x,1}^2 + 2n_{x,1}\lambda_* q_{16}d_{x,1} + 2n_{y,1}\lambda_* q_{6}d_{x,1} + a_1\bar{k}_1 + a_3\bar{k}_3 + a_4\bar{k}_4 + a_6\bar{k}_6 + a_7\bar{k}_7 + a_9\bar{k}_9 \\ &+ 2d_{x,5}n_{y,5}\mu_* q_{10} + d_{x,2}^2q_{12} + d_{x,3}^2q_{13} + d_{x,4}^2q_{14} + d_{x,5}^2q_{15} + 2d_{x,2}n_{x,2}\mu_* q_{17} \\ &+ 2d_{x,3}n_{x,3}\mu_* q_{18} + 2d_{x,4}n_{x,4}\mu_* q_{19} + 2d_{x,5}n_{x,5}\mu_* q_{20} + 2d_{x,2}n_{y,2}\mu_* q_7 + 2d_{x,3}n_{y,3}\mu_* q_8 + 2d_{x,4}n_{y,4}\mu_* q_9)(f_{G,y}^*)) \\ &+ \frac{1}{2(\lambda_{**} + 2\mu_{***})} ((q_1d_{x,1}^2 + 2\lambda_{**}n_{y,1}q_{16}d_{x,1} + 2\lambda_{**}n_{x,1}q_6d_{x,1} + 4n_{x,1}\mu_* q_6d_{x,1} \\ &+ (a_1 - 1)k_1 + (a_3 - 1)k_3 + a_4k_4 - k_4 + a_6k_6 - k_6 + a_7k_7 - k_7 + a_9k_9 \\ &- k_9 + 2d_{x,5}\lambda_* n_{x,5}q_{10} + d_{x,5}n_{x,5}\mu_* q_{10} + 2d_{x,2}\lambda_* n_{y,2}q_{17} + 2d_{x,3}\lambda_* n_{y,3}q_{18} \\ &+ 2d_{x,4}\lambda_* n_{y,4}q_{19} + d_{x,2}^2q_{2} + 2d_{x,5}\lambda_* n_{y,5}q_{20} + d_{x,3}^2q_3 + d_{x,4}^2q_4 + d_{x,5}^2q_5 \\ &+ 2d_{x,2}\lambda_* n_{x,2}q_7 + d_{x,2}n_{x,2}\mu_* q_7 + 2d_{x,3}\lambda_* n_{x,3}q_8 + d_{x,3}n_{x,3}\mu_* q_8 + 2d_{x,4}\lambda_* n_{x,4}q_9 + 4d_{x,4}n_{x,4}\mu_* q_9)(f_{G,x}^{**})) \\ &+ \frac{1}{2\mu_*} ((q_{11}d_{x,1}^2 + 2n_{x,1}\mu_* q_{16}d_{x,1} + 2n_{y,1}\mu_* q_6d_{x,1} + (a_1 - 1)\bar{k}_1 + (a_3 - 1)\bar{k}_3 \\ &+ a_4\bar{k}_4 - \bar{k}_4 + a_6\bar{k}_6 - \bar{k}_6 + a_7\bar{k}_7 - \bar{k}_7 + a_9\bar{k}_9 - \bar{k}_9 + 2d_{x,5}n_{y,5}p_{**}q_{10} \\ &+ d_{x,2}^2q_{12} + d_{x,3}^2q_{13} + d_{x,4}^2q_{14} + d_{x,5}^2q_{15} + 2d_{x,2}n_{x,2}\mu_* q_{17} + 2d_{x,3}n_{x,3}\mu_* q_$$

as well as we will get the same local truncation errors $e_1^f = e_1$ for zero and non-zero body forces (see the attached file 'RHS.nb' for the detailed expression of $\bar{f}_{1.5}$). This means that the coefficients $k_{j,i}$, $\bar{k}_{j,i}$ ($i=1,2,...,9,\ j=1,2$) of the stencil equations are first calculated for zero body forces $f_x^* = f_x^{**} = f_y^* = f_y^{**} = 0$ as described in Section 2.1. Then, the nonzero term $f_{1,5}$ given by Eq. (32) is used in the stencil equation, Eq. (11) for nonzero body forces.

Remark 10. The derivation of the term $f_{2,5}$ for the second stencil equation, Eq. (11), with j=2 can be done similar to that for $f_{1,5}$. To preserve symmetry in the derivations for the first and second stencils with respect to the x and y coordinates, for the second stencil with j = 2, Eqs. (16)–(19) (with the corresponding modifications of Eqs. (20)–(23)) should express the second y derivatives in terms of the second x derivatives and the second mixed derivatives (see the Remark 6).

3. Numerical examples

In this section, the computational efficiency of OLTEM developed for the 2-D time-independent elasticity interface problems will be demonstrated and compared with conventional linear (triangular T3 and quadrilateral Q4), quadratic (triangular T6 and quadrilateral Q9), and cubic (triangular T10 and quadrilateral Q16) finite elements. The commercial finite element software 'COMSOL' is used for the finite element simulations. Similar to FEM terminology, a grid point of a Cartesian mesh will be called a node. In order to compare the accuracy of the numerical results obtained by OLTEM and by FEM, the relative error e_s^j at the jth node and the maximum relative error e_s^{max} for the variable s are defined as:

$$e_s^j = \frac{|s_j^{num} - s_j^{exact}|}{s_{max}^{exact}}$$
, $e_s^{max} = \max_j e_s^j$, $j = 1, 2, ..., N$.

In Eq. (33) the superscripts 'num' and 'exact' correspond to the numerical and exact solutions, N is the total number of nodes used in calculations, s_{max}^{exact} is the maximum absolute value of the exact solution for the variable s over the entire domain. We also use the relative error e_s^{L} in the L^2 norm

3.1. A square plate with a vertical interface

Let us consider a square plate *AEBCFD* with dimensions 2×2 ; see Figure 2(a). A vertical interface *EF* at x=0 divides the domain Ω into two subdomains: *AEFD* (subdomain Ω_I) and *EBCF* (subdomain Ω_{II}). For the vertical interface the components of the unit normal used in the interface conditions equal $n_x = 1$ and $n_y = 0$ for all interface points. Young's modulus *E* and Poisson's ratio ν are selected to be $E_I = 1$, $\nu_I = 0.3$ for Ω_I (*AEFD*) and $E_{II} = 0.5$, $\nu_{II} = 0.4$ for Ω_{II} (*EBCF*). The Lame coefficients can be calculated as $\lambda_i = \frac{E_i \nu_i}{(1+\nu_i)(1-2\nu_i)}$ and $\mu_i = \frac{E_i}{2(1+\nu_i)}$ with i = I, II. Using the method of manufactured solutions, the following exact solution (e.g., see [45]) is selected (this solution meets the interface conditions, Eqs. (3) and (4)):

$$\begin{split} u_I(x,y) &= \frac{x}{\lambda_I + 2\mu_I} \cos{(4xy)}, \quad v_I(x,y) = \frac{x}{\mu_I} \cos{(4xy)} \text{ in } \Omega_I \\ u_{II}(x,y) &= \frac{x}{\lambda_{II} + 2\mu_{II}} \cos{(2xy)}, \quad v_{II}(x,y) = \frac{x}{\mu_{II}} \cos{(2xy)} \text{ in } \Omega_{II} \ . \end{split}$$

The body forces can be calculated by the substitution of the exact solution into the elasticity equations and are given below:

$$\begin{cases} f_x^I(x,y) = \frac{8(\sin{(4xy)}(x\lambda_I + (x+y)\mu_I) + \frac{2x\cos{(4xy)}(xy\lambda_I^2 + y(3x+y)\lambda_1\mu_I + (x^2 + 2xy + 2y^2)\mu_I^2)}{\mu_I}}{\mu_I}, & \text{in } \Omega_I \\ f_y^I(x,y) = \frac{8\sin{(4xy)}\mu_I((x+y)\lambda_I + (x+2y)\mu_I) + 16x\cos{(4xy)}(x^2\lambda_I^2 + (4x^2 + xy + y^2)\lambda_I\mu_I + (4x^2 + xy + 2y^2)\mu_I^2)}{\mu_I(\lambda_I + 2\mu_I)}, \\ f_x^{II}(x,y) = \frac{4(\sin{(2xy)}(x\lambda_{II} + (x+y)\mu_{II}) + \frac{x\cos{(2xy)}(xy\lambda_{II}^2 + y(3x+y)\lambda_{II}\mu_I + (x^2 + 2xy + 2y^2)\mu_{II}^2)}{\lambda_{II} + 2\mu_{II}}}{\mu_{II}}, & \text{in } \Omega_{II} \\ f_y^{II}(x,y) = \frac{4\sin{(2xy)}\mu_{II}((x+y)\lambda_{II} + (x+2y)\mu_{II}) + 4x\cos{(2xy)}(x^2\lambda_{II}^2 + (4x^2 + xy + y^2)\lambda_{II}\mu_{II} + (4x^2 + xy + 2y^2)\mu_{II}^2)}{\mu_{II}(\lambda_{II} + 2\mu_{II})}. \end{cases}$$

for finite elements (e.g., see [43]) and the relative error $e_s^{l^2}$ in the l^2 norm (e.g., see [44]) for OLTEM:

$$e_s^P = \frac{||s^{exact} - s^{num}||_P}{||s^{exact}||_{L^2}},$$
 (34)

where $||s^{exact} - s^{num}||_p = \{dx \ dy \ \sum_{i=0}^{N_x} \sum_{j=0}^{N_y} [s^{exact} \ (x_i, y_j) - s^{num}(x_i, y_j)]^2\}^{\frac{1}{2}}$. N_x and N_y are the numbers of Cartesian grid points along the x and y axes, x_i and y_j are the coordinates of Cartesian grid points. The displacements u and v are considered as variable s in Eqs. (33) and (34).

The numerical examples presented in this section are organized as follows. First, a test problem with a vertical interface is solved in Section 3.1. Then, a more complicated circular interface problem is considered in Section 3.2.

The test problem is solved by OLTEM as well as by conventional linear, quadratic and cubic finite elements on square ($b_y = 1$) Cartesian meshes. The Dirichlet boundary conditions are imposed along the edges of the square plate according to the exact solution, Eq. (35). Figure 2(c,d) shows the distribution of the relative errors e_u (Figure 2(c)) and e_v (Figure 2(d)) obtained by OLTEM on the mesh with size h = 1/64. As can be seen from Figure 2(c,d), the errors are very small for this mesh; i.e., OLTEM yields accurate results.

In order to compare the accuracy of the numerical solutions obtained by different techniques, Figure 3 shows the maximum relative errors e_u^{max} , e_v^{max} and the errors $e_u^{L^2}$, $e_v^{L^2}$ in the L^2 norm as a function of the mesh size h. As can be seen from Figure 3, at the same h the numerical results obtained by OLTEM are much more accurate than those obtained by linear finite elements; compare curves 1 and 2.

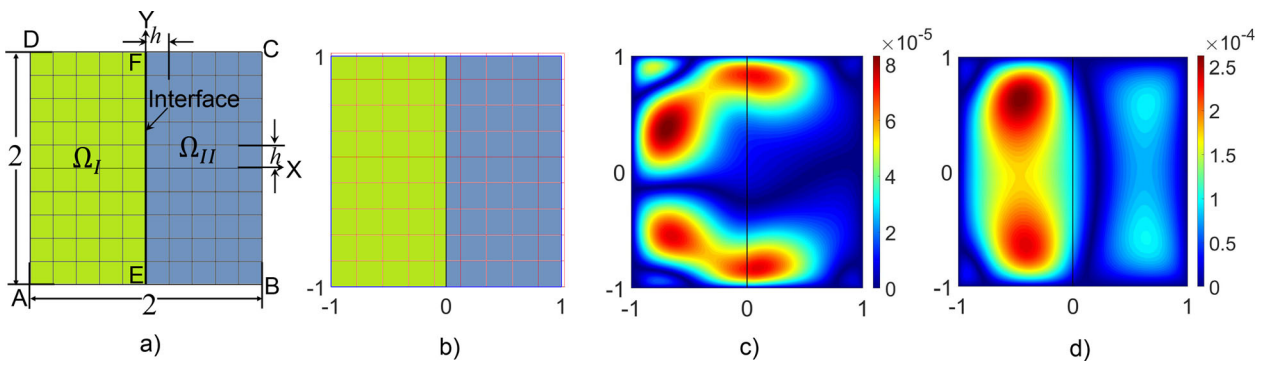


Figure 2. A square plate AEBCFD with a vertical interface EF at x = 0. Examples of a fitted Cartesian mesh (a) used by finite elements and OLTEM as well as an unfitted Cartesian mesh (b) used by OLTEM. The distribution of the relative errors e_u (c) and e_v (d) obtained by OLTEM on a square Cartesian mesh with size h = 1/64.

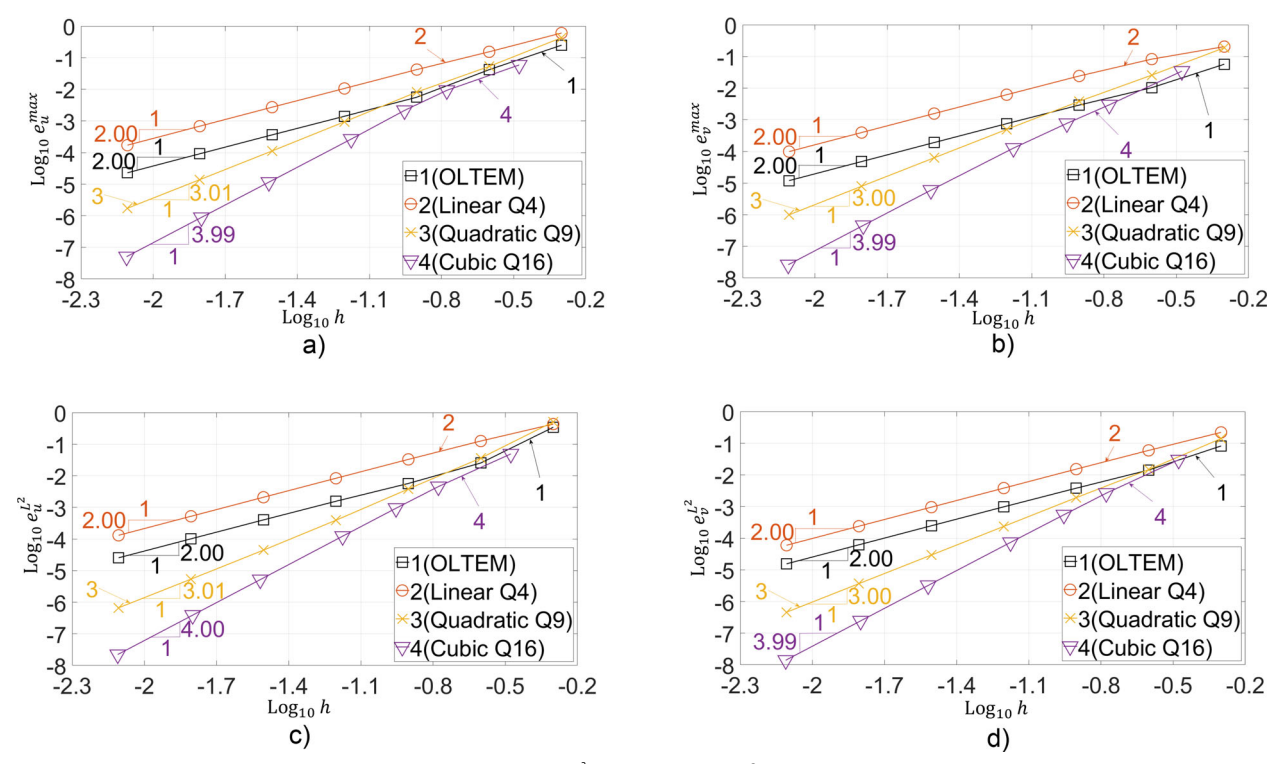


Figure 3. The maximum relative errors e_u^{max} (a), e_v^{max} (b); and the errors $e_v^{l^2}$ (c), $e_v^{l,2}$ (d) in the l^2 norm as a function of the mesh size h in the logarithmic scale. The numerical solutions for the test problem with the vertical interface are obtained by OLTEM (curve 1) and by conventional linear (curve 2), quadratic (curve 3), and cubic (curve 4) quadrilateral finite elements on square Cartesian meshes.

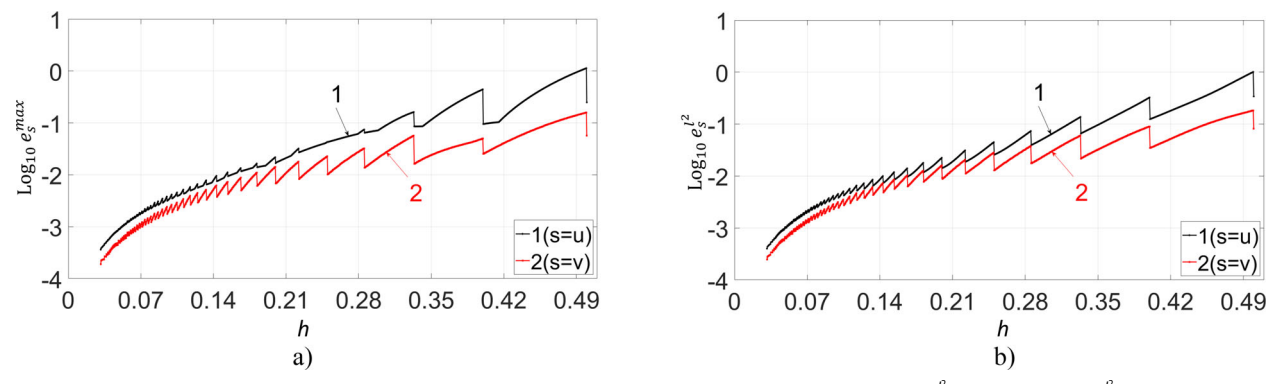


Figure 4. The logarithm of the maximum relative errors e_u^{max} (curve 1 in (a)), e_v^{max} (curve 2 in (a)) and the errors e_u^{f} (curve 1 in (b)), e_v^{f} (curve 2 in (b)) in the f^2 norm as a function of the mesh size f. The numerical solutions for the test problem with the vertical interface are obtained by OLTEM on square Cartesian meshes.

In addition to that, up to the engineering accuracy of 1% (-2 along the y-axis in Figure 3 corresponds to 1%), OLTEM yields more accurate results than those for

quadratic finite elements and the results that are close to those for cubic finite elements at the same mesh size. The increase in accuracy by OLTEM is impressive considering

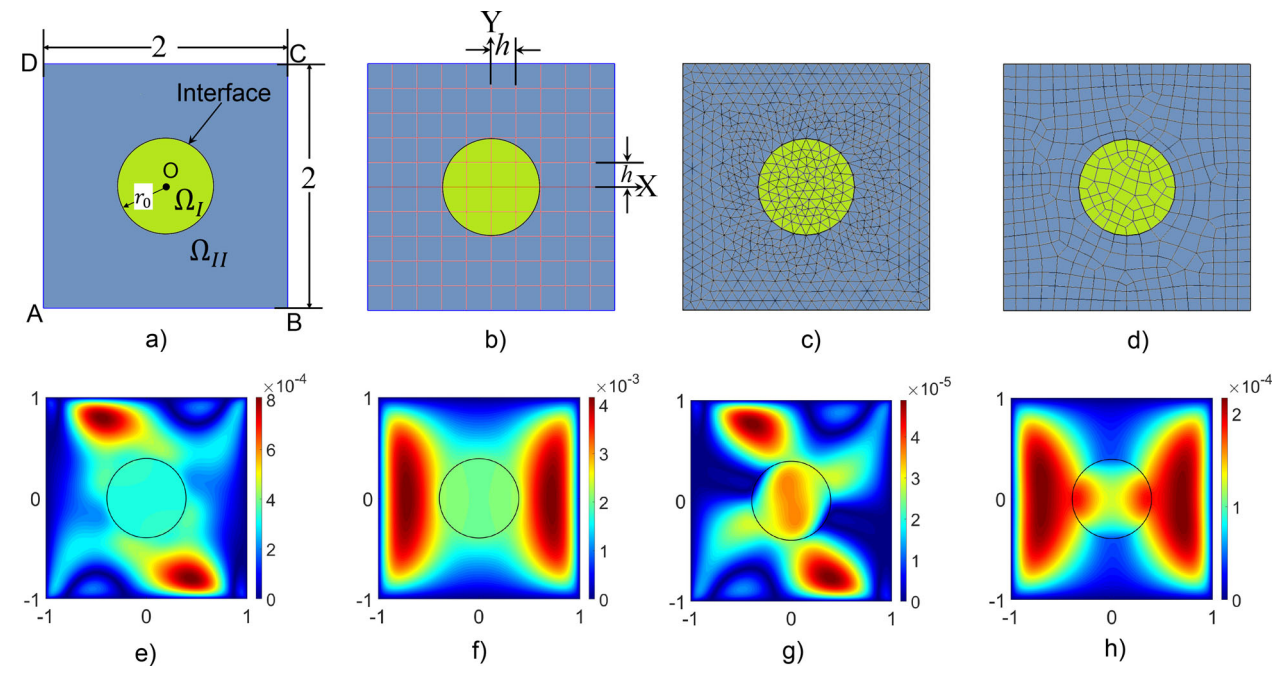


Figure 5. A square plate ABCD with a circular interface centered at O(0, 0) with a radius $r_0 = \pi/8$ (a). Examples of a square Cartesian mesh for OLTEM (b), of triangular (c), and quadrilateral (d) finite element meshes generated by COMSOL. The distribution of the relative errors e_u (e, g) and e_v (f, h) obtained by OLTEM on a square Cartesian mesh with size h = 1/64. The contrasts $E_c = 20$ (e, f) and $E_c = \frac{1}{20}$ (g, h) are used.

the fact that quadratic and cubic finite elements have much wider stencils compared to those for OLTEM (the width of the stencils for OLTEM corresponds to that for linear quadrilateral finite elements). This means that up to the engineering accuracy, OLTEM requires less computation time compared to that for conventional finite elements up to the third order on conformed meshes. The slopes of the curves in Figure 3 correspond to the order of convergence of the corresponding numerical techniques. As can be seen from Figure 3, OLTEM provides the second order of convergence at mesh refinement that is in agreement with the theoretical results of Section 2.

In order to study, the convergence and stability of the numerical results obtained by OLTEM in more detail, Figure 4 presents the curves 1 in Figure 3 at small changes of the mesh size h (curves 1 and 2 in Figure 4(a) correspond to curves 1 in Figure 3(a,b); curves 1 and 2 in Figure 4(b) correspond to curves 1 in Figure 3(c,d)). For this study, we solve the test problem on 1001 Cartesian meshes with the mesh sizes $h_i = h_1 + \frac{(h_2 - h_1)(i-1)}{1000}$ where $h_1 = 1/2 = 0.5$, $h_2 = 1/32 = 0.03125$ and i = 1, 2, ..., 1001. The grid lines of these meshes along the sides AB and AD (see Figure 2(a)) are fixed; i.e., almost all meshes and the interface are unfitted as in Figure 2(b). As can be seen from Figure 4, the numerical results obtained by OLTEM on these meshes converge with the decrease in the grid size h. Small oscillations in Figure 4 decrease with the decrease in the mesh size. This oscillatory behavior can be explained by the fact that at small variations of the mesh size h, there is a discontinuous change in the location of the grid points with respect to the interface (e.g., some grid points that belong to one material for the previous mesh can belong to another material for the next mesh); this leads to the discontinuous change of some stencils equations for the meshes with a small difference in h. It

is important to mention that small oscillations in numerical convergence curves are typical for many numerical techniques at small variations of h. For example, the change in the angles of finite elements at small variations of the element size h also leads to such oscillations in convergence curves for finite element techniques.

3.2. A square plate with a circular interface

Let us consider a square plate *ABCD* with dimensions 2×2 ; see Figure 5. A circular interface with radius $r_0 = \pi/8$ centered at the origin O(0, 0) divides the domain Ω into two subdomains: the circular subdomain Ω_I and the remaining subdomain Ω_{II} . For the circular interface, the components of the unit normal used in the interface conditions equal $n_x = \frac{x}{r_0}$ and $n_y = \frac{y}{r_0}$ for any interface point with the coordinates (x, y). Using the method of manufactured solutions, the following exact solution (e.g., see [45]) is selected:

$$\begin{cases} u_{I}(x,y) = \frac{\left(\sqrt{r^{2}+1}\right)^{\alpha}}{\lambda_{I}}, & \text{in } \Omega_{I} \\ v_{I}(x,y) = \frac{\left(\sqrt{r^{2}+1}\right)^{\beta}}{\lambda_{I}}, & \text{in } \Omega_{I} \end{cases}$$

$$\begin{cases} u_{II}(x,y) = \frac{\left(\sqrt{r^{2}+1}\right)^{\alpha}}{\lambda_{II}} + \left(\frac{1}{\lambda_{I}} - \frac{1}{\lambda_{II}}\right) \left(\sqrt{r_{0}^{2}+1}\right)^{\alpha}, & \text{in } \Omega_{II} \\ v_{II}(x,y) = \frac{\left(\sqrt{r^{2}+1}\right)^{\beta}}{\lambda_{II}} + \left(\frac{1}{\lambda_{I}} - \frac{1}{\lambda_{II}}\right) \left(\sqrt{r_{0}^{2}+1}\right)^{\beta}, & \text{in } \Omega_{II} \end{cases}$$

where $\alpha = 7$, $\beta = 10$, and $r = \sqrt{x^2 + y^2}$. The body forces can be calculated by the substitution of the exact solution into the elasticity equations and are given below:



$$\begin{cases} f_x^I(x,y) = -\frac{xy\big(\sqrt{r^2+1}\big)^\beta(-2+\beta)\beta(\lambda_I+\mu_I) + \big(\sqrt{r^2+1}\big)^\alpha\alpha((1+y^2+x^2(-1+\alpha))\lambda_I + (3+y^2(1+\alpha)+x^2(-1+2\alpha))\mu_I)}{(1+r^2)^2\lambda_I} , & \text{in } \Omega_I \\ f_y^I(x,y) = -\frac{xy\big(\sqrt{r^2+1}\big)^\alpha(-2+\alpha)\alpha(\lambda_I+\mu_I) + \big(\sqrt{r^2+1}\big)^\beta\beta((1+x^2+y^2(-1+\beta))\lambda_I + (3+x^2(1+\beta)+y^2(-1+2\beta))\mu_I)}{(1+r^2)^2\lambda_I} , & \text{in } \Omega_I \\ f_x^{II}(x,y) = -\frac{xy\big(\sqrt{r^2+1}\big)^\beta(-2+\beta)\beta(\lambda_{II}+\mu_{II}) + \big(\sqrt{r^2+1}\big)^\alpha\alpha((1+y^2+x^2(-1+\alpha))\lambda_{II} + (3+y^2(1+\alpha)+x^2(-1+2\alpha))\mu_{II})}{(1+r^2)^2\lambda_I} , & \text{in } \Omega_{II} \\ f_y^{II}(x,y) = -\frac{xy\big(\sqrt{r^2+1}\big)^\alpha(-2+\alpha)\alpha(\lambda_{II}+\mu_{II}) + \big(\sqrt{r^2+1}\big)^\beta\beta((1+x^2+y^2(-1+\beta))\lambda_{II} + (3+x^2(1+\beta)+y^2(-1+2\beta))\mu_{II})}{(1+r^2)^2\lambda_I} . \end{cases}$$

Six different combinations of Lame's coefficients λ and μ are used to solve this problem by OLTEM: 1) $\lambda_I = 10$, $\lambda_{II} =$ 5, $\mu_I = 4$, $\mu_{II} = 2$; 2) $\lambda_I = 100$, $\lambda_{II} = 5$, $\mu_I = 40$, $\mu_{II} = 2$; 3) $\lambda_{I} = 1000, \ \lambda_{II} = 5, \ \mu_{I} = 400, \ \mu_{II} = 2;$ 4) $\lambda_{I} = 5, \ \lambda_{II} = 5$ 10, $\mu_I = 2$, $\mu_{II} = 4$; 5) $\lambda_I = 5$, $\lambda_{II} = 100$, $\mu_I = 2$, $\mu_{II} = 40$ and 6) $\lambda_I = 5$, $\lambda_{II} = 1000$, $\mu_I = 2$, $\mu_{II} = 400$. They correspond to the same Poisson's ratio $\nu_I = \nu_{II} = \frac{5}{14} = 0.357$ and following Young's $\frac{76}{7}; \frac{760}{7}; \frac{7600}{7}; \frac{38}{7}; \frac{38}{7}; \frac{38}{7}; \frac{38}{7}; \frac{38}{7}; \frac{38}{7}; \frac{38}{7}; \frac{760}{7}; \frac{7600}{7}$ with the following contrasts for Young's moduli: $E_c = \frac{E_I}{E_{II}} = \frac{1}{2}$ $2;20;200;\frac{1}{2};\frac{1}{20};\frac{1}{200}$. The exact solution given by Eqs. (36) with the selected material properties meets the interface conditions, Eqs. (3) and (4).

The test problem is solved by OLTEM on square ($b_y =$ 1) Cartesian meshes as well as by conventional linear, quadratic, and cubic (triangular and quadrilateral) finite elements; see Figure 5(b) for an example of Cartesian mesh used with OLTEM and see Figure 5(c,d) for examples of triangular and quadrilateral finite element meshes generated by COMSOL. The Dirichlet boundary conditions are imposed along the edges of the square plate according to the exact solution given by Eq. (36). Figure 5(e-h) shows the distribution of the relative errors e_u (5e,g) and e_v (5f,h) obtained by OLTEM on a square Cartesian mesh with size h=1/64. The contrasts $E_c=20$ and $E_c=\frac{1}{20}$ are used for the results shown in Figure 5(e-h). As can be seen from Figure 5(e-h) the errors are very small for this mesh; i.e., OLTEM yields accurate results.

In order to study, the convergence of the numerical results obtained by OLTEM for different contrasts E_c , Figure 6 shows the maximum relative errors e_u^{max} , e_v^{max} and the errors $e_{\nu}^{l^2}$, $e_{\nu}^{l^2}$ in the l^2 norm as a function of the mesh size h in the logarithmic scale. The slopes of the curves in Figure 6 correspond the order of convergence. As can be seen from Figure 6, OLTEM provides the second order of convergence for all selected contrasts E_c . This is in agreement of the theoretical results of Section 2.

In order to compare the accuracy of the numerical solutions obtained by different techniques, Figure 7 shows the maximum relative errors e_u^{max} , e_v^{max} and the errors $e_u^{L^2}$, $e_v^{L^2}$ in the L^2 norm as a function of the number N of degrees of freedom for the contrast $E_c = \frac{1}{20}$. As can be seen from Figure 7, at the same h the numerical results obtained by OLTEM are much more accurate than those obtained by linear finite elements; compare curve 1 with curves 2 and 5. In addition to that, up to the engineering accuracy of 1% (-2 along the y-axis in Figure 7 corresponds to 1%), OLTEM yields more accurate results than those for quadratic and cubic finite elements at the same N. The increase in accuracy by OLTEM is impressive considering the fact that the quadratic and cubic finite elements have much wider stencils compared to those for OLTEM (the width of the stencils for OLTEM corresponds to that for linear quadrilateral finite elements). This means that at the engineering accuracy, OLTEM requires less computation time compared to that for conventional finite elements up to the third order on conformed meshes. We should mention that similar numerical results and comparison with finite elements are obtained for different contrasts E_c .

Similar to Figure 4 in Section 3.1, in order to study the convergence and stability of the numerical results obtained by OLTEM in more detail, Figure 8 presents the curves 1 in Figure 7 at small changes of the mesh size h (curves 1 and 2 in Figure 8(a) correspond to curves 1 in Figure 7(a,b); curves 1 and 2 in Figure 8(b) correspond to curves 1 in Figure 7(c,d)). For this study, we solve the test problem on 1001 Cartesian meshes with the mesh sizes $h_i = h_1 +$ $\frac{(h_2 - h_1)(i-1)}{1000}$ where $h_1 = 1/4 = 0.25$, $h_2 = 1/64 = 0.015625$ and i = 1, 2, ..., 1001. As can be seen from Figure 8, the numerical results obtained by OLTEM converge with the decrease in the grid size h. Small oscillations in the convergence curves in Figure 8 can be explained similar to those in Figure 4. The amplitudes of these oscillations decrease with the decrease in the mesh size. The detailed numerically study presented in Figures 4 and 8 show that the solutions obtained by OLTEM are stable and convergent.

It can be concluded that OLTEM developed for the 2D time-independent elasticity interface problems, yields more accurate results than linear finite elements with the same width of the stencil equations. Moreover, at engineering accuracy, OLTEM requires less computational costs than those for quadratic and cubic finite elements.

4. Concluding remarks

OLTEM for the time-independent elasticity equations with irregular interfaces developed in this article is the extension of the technique considered in our article [36] for the time-



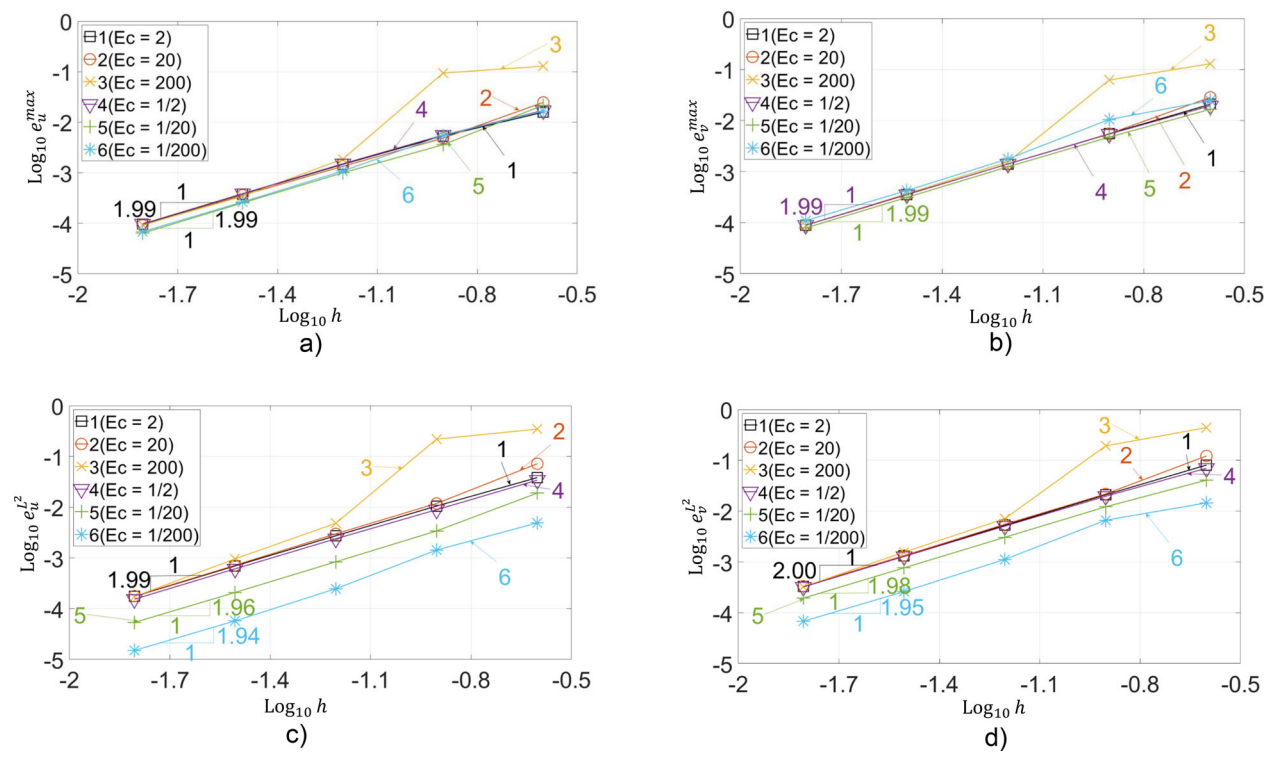


Figure 6. The maximum relative errors e_u^{max} (a), e_v^{max} (b) and the errors e_u^{l} (c), e_v^{l} (d) in the l^2 norm as a function of the mesh size h in the logarithmic scale. The numerical solutions for the test problem with the circular interface are obtained by OLTEM on square Cartesian meshes with the following contrasts: $E_c = 2$ (curve 1); $E_c = 20$ (curve 2); $E_c = 200$ (curve 3); $E_c = \frac{1}{2}$ (curve 4); $E_c = \frac{1}{20}$ (curve 5) and $E_c = \frac{1}{200}$ (curve 6).

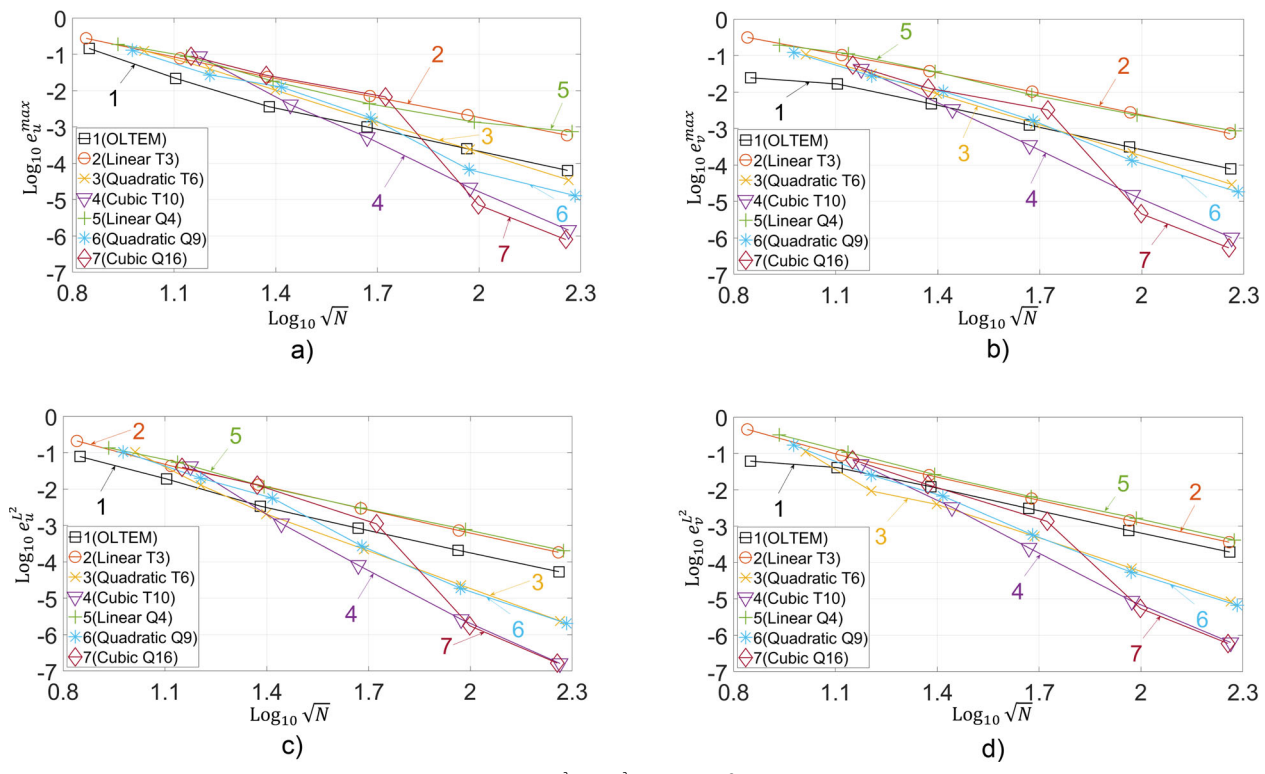
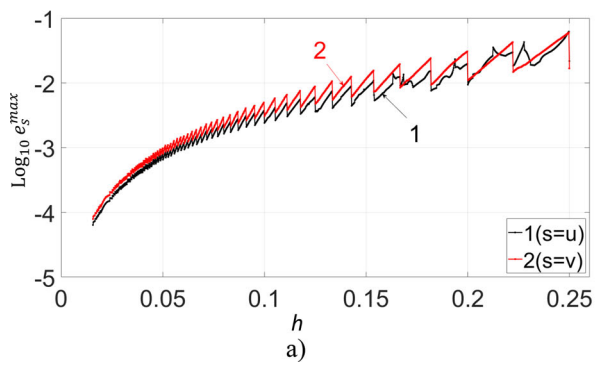


Figure 7. The maximum relative errors e_u^{max} (a), e_v^{max} (b) and the errors $e_u^{l,l}$ (c), $e_v^{l,l}$ (d) in the L^2 norm as a function of the N in the logarithmic scale (N is the number of degrees of freedom). The numerical solutions for the plate with the circular interface are obtained by OLTEM (curve 1) and by conventional linear (curves 2 and 5), quadratic (curves 3 and 6), and cubic (curves 4 and 7) finite elements with triangular (curves 2–4) and quadrilateral (curves 5–7) elements. The contrast $E_c = \frac{1}{20}$ is used.

dependent scalar wave and heat equations. Due to the absence of the time variable, the stencil equations, the derivations as well as the imposition of the interface conditions

for OLTEM are different for the elasticity equations compared to those in our article [36] (see also the Introduction). Nevertheless, OLTEM developed for the elasticity equations



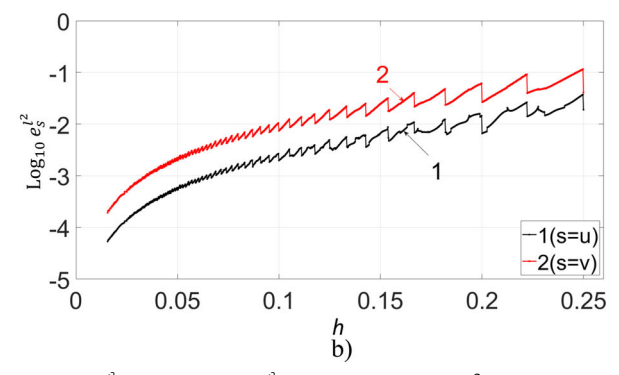


Figure 8. The maximum relative errors e_u^{max} (curve 1 in (a)), e_v^{max} (curve 2 in (a)) and the errors $e_v^{l^2}$ (curve 1 in (b)), $e_v^{l^2}$ (curve 2 in (b)) in the l^2 norm as a function of the mesh size h in the logarithmic scale. The numerical solutions for the plate with the circular interface are obtained by OLTEM on 1001 square Cartesian meshes for the contrast $E_c = \frac{1}{20}$.

shares many advantages of OLTEM developed in our article [36] for the time-dependent PDEs. One of the ideas that allow the effective development of the new technique for heterogeneous materials is the addition of the interface conditions at a small number of the interface points to the expression for the local truncation error. The unknown stencil coefficients of OLTEM are numerically calculated from a small local system of algebraic equations for the general geometry of interfaces. This procedure does not change the width of the stencil equation; i.e., the locations of zero and nonzero elements in the global discrete system of equations are the same for homogeneous and heterogeneous materials. The calculation of the unknown stencil coefficients is based on the minimization of the local truncation error of the stencil equations and yields the optimal order of accuracy of the new technique at a given stencil width. The increase in the computational costs for the calculation of the unknown stencil coefficients from the local systems is insignificant compared to the computational costs for the solution of the global discrete system.

The main advantages of the suggested technique can be summarized as follows:

- Many difficulties of the existing numerical techniques for irregular domains (e.g., finite elements, spectral element, isogeometric elements, the finite volume method, and many other) are related to complicated mesh generators and the accuracy of 'bad' elements (e.g., the elements with small angles). In contrast to these techniques, OLTEM is based on simple unfitted Cartesian meshes with a trivial procedure for the formation of the 9-point stencils for 2D domains with complex irregular interfaces.
- OLTEM has the same width of the stencil equations and the same structure of the global discrete equations for the elasticity equations for homogeneous and heterogeneous materials. There are no unknowns on the interfaces between different materials for the proposed technique; i.e., complex irregular interfaces do not affect the sparse structure of the global system of discrete equations (they affect just the values of the stencils coefficients).
- In contrast to the finite-difference techniques with the stencil coefficients calculated through the approximation of the partial derivatives, the system of partial differential

elasticity equations is used for the calculation of the stencil coefficients in OLTEM. This leads to the optimal accuracy of the proposed technique. E.g., the 9-point stencils of OLTEM provide the optimal second order of accuracy that cannot be improved without changing the width of stencil equations. The numerical results with irregular interfaces show that at the same number of degrees of freedom: a) OLTEM with unfitted Cartesian meshes is more accurate than linear finite elements with similar stencils and conformed meshes; b) up to engineering accuracy of 1%, OLTEM with unfitted Cartesian meshes is even more computationally efficient than quadratic and cubic finite elements with much wider stencils and conformed meshes.

- OLTEM does not require time-consuming numerical integration for finding the coefficients of the stencil equations; e.g., as for the high-order finite, spectral, and isogeometric elements. The stencil coefficients are calculated analytically or numerically (for the general geometry of interfaces) by the solution of small local systems of linear algebraic equations. Numerical experiments show that the solution of these small local systems of algebraic equations is fast. Moreover, these local systems are independent of each other and can be efficiently solved on a parallel computer.
- The proposed technique yields accurate numerical results for heterogeneous materials with big contrasts in the material properties of different components.
- Due to the computational efficiency and trivial unfitted Cartesian meshes that are independent of irregular geometry, the proposed technique does not require remeshing for the shape change of irregular geometry and it will be effective for many design and optimization problems.

In the future, we plan to extend OLTEM to the 3D elasticity equations for heterogeneous materials with irregular interfaces. Another direction is the development of OLTEM with adaptive refinement similar to h- and p- refinement for finite elements (e.g., it was shown in our articles [46,47] that OLTEM can easily combine different stencils). We plan to use quadtrees/octrees meshes that allow a simple refinement strategy with Cartesian meshes. The extension of OLTEM to other PDEs for heterogeneous materials as well as to non-linear PDEs will be also considered in the future.

Acknowledgments

The views and conclusions contained in this article are those of the authors and should not be interpreted as representing the official policies.

Funding

The research of AI (theoretical developments), BD (numerical study), and MM (numerical study) has been supported in part by the Army Research Office (Grant Number W911NF-21-1-0267), the NSF grant CMMI-1935452 and by Texas Tech University.

References

- [1] K. Singh, and J. Williams, A parallel fictitious domain multigrid preconditioner for the solution of Poisson's equation in complex geometries, Comput. Methods Appl. Mech. Eng., vol. 194, no. 45–47, pp. 4845–4860, 2005. DOI: 10.1016/j.cma.2005.01.003.
- [2] P. Vos, R. van Loon, and S. Sherwin, A comparison of fictitious domain methods appropriate for spectral/hp element discretisations, Comput. Methods Appl. Mech. Eng., vol. 197, no. 25–28, pp. 2275–2289, 2008. DOI: 10.1016/j.cma.2007.11.023.
- [3] E. Burman, and P. Hansbo, Fictitious domain finite element methods using cut elements: I. a stabilized lagrange multiplier method, Comput. Methods Appl. Mech. Eng., vol. 199, no. 41–44, pp. 2680–2686, 2010. DOI: 10.1016/j.cma.2010.05.011.
- [4] E. Rank, S. Kollmannsberger, C. Sorger, and A. Duster, Shell finite cell method: A high order fictitious domain approach for thin-walled structures, Comput. Methods Appl. Mech. Eng., vol. 200, no. 45–46, pp. 3200–3209, 2011. DOI: 10.1016/j.cma.2011. 06.005.
- [5] E. Rank, M. Ruess, S. Kollmannsberger, D. Schillinger, and A. Duster, Geometric modeling, isogeometric analysis and the finite cell method, Comput. Methods Appl. Mech. Eng., vol. 249–252, pp. 104–115, 2012. DOI: 10.1016/j.cma.2012.05.022.
- [6] T. Fries, S. Omerović, D. Schöllhammer, and J. Steidl, Higher-order meshing of implicit geometries—part i: Integration and interpolation in cut elements, Comput. Methods Appl. Mech. Eng., vol. 313, pp. 759–784, 2017. DOI: 10.1016/j.cma.2016.10.019.
- [7] T. Hoang, C. V. Verhoosel, F. Auricchio, E. H. van Brummelen, and A. Reali, Mixed isogeometric finite cell methods for the stokes problem, Comput. Methods Appl. Mech. Eng., vol. 316, pp. 400–423, 2017. DOI: 10.1016/j.cma.2016.07.027.
- [8] S. Zhao, and G. W. Wei, Matched interface and boundary (mib) for the implementation of boundary conditions in highorder central finite differences, Int. J. Numer. Methods Eng., vol. 77, no. 12, pp. 1690–1730, 2009. DOI: 10.1002/nme.2473.
- [9] S. May, and M. Berger, An explicit implicit scheme for cut cells in embedded boundary meshes, J. Sci. Comput., vol. 71, no. 3, pp. 919–943, 2017. DOI: 10.1007/s10915-016-0326-2.
- [10] H. O. Kreiss, and N. A. Petersson, An embedded boundary method for the wave equation with discontinuous coefficients, SIAM J. Sci. Comput., vol. 28, no. 6, pp. 2054–2074, 2006. DOI: 10.1137/050641399.
- [11] H. O. Kreiss, and N. A. Petersson, A second order accurate embedded boundary method for the wave equation with Dirichlet data, SIAM J. Sci. Comput., vol. 27, no. 4, pp. 1141–1167, 2006. DOI: 10.1137/040604728.
- [12] H. O. Kreiss, N. A. Petersson, and J. Ystrom, Difference approximations of the Neumann problem for the second order wave equation, SIAM J. Numer. Anal., vol. 42, no. 3, pp. 1292–1323, 2004. DOI: 10.1137/S003614290342827X.
- [13] Z. Jomaa, and C. Macaskill, The shortley-weller embedded finite-difference method for the 3d Poisson equation with mixed boundary conditions, Comput. Phys., vol. 229, no. 10, pp. 3675–3690, 2010. DOI: 10.1016/j.jcp.2010.01.021.
- [14] Z. Jomaa, and C. Macaskill, The embedded finite difference method for the Poisson equation in a domain with an irregular

- boundary and Dirichlet boundary conditions, Comput. Phys., vol. 202, no. 2, pp. 488–506, 2005. DOI: 10.1016/j.jcp.2004.07.011.
- [15] H. Jeffrey Lee, Jr., L. Wang, E. Sifakis, and J. M. Teran, A second order virtual node method for elliptic problems with interfaces and irregular domains in three dimensions, Comput. Phys. ., vol. 231, no. 4, pp. 2015–2048, 2012. DOI: 10.1016/j.jcp. 2011.11.023.
- [16] L. Chen, H. Wei, and M. Wen, An interface-fitted mesh generator and virtual element methods for elliptic interface problems, Comput. Phys., vol. 334, pp. 327–348, 2017. DOI: 10.1016/j.jcp. 2017.01.004.
- [17] J. Bedrossian, J. H. von Brecht, S. Zhu, E. Sifakis, and J. M. Teran, A second order virtual node method for elliptic problems with interfaces and irregular domains, Comput. Phys., vol. 229, no. 18, pp. 6405–6426, 2010. DOI: 10.1016/j.jcp.2010.05. 002.
- [18] D. C. Assêncio, and J. M. Teran, A second order virtual node algorithm for stokes flow problems with interfacial forces, discontinuous material properties and irregular domains, Comput. Phys., vol. 250, pp. 77–105, 2013. DOI: 10.1016/j.jcp.2013.04. 041.
- [19] K. Mattsson, and M. Almquist, A high-order accurate embedded boundary method for first order hyperbolic equations, Comput. Phys., vol. 334, pp. 255–279, 2017. DOI: 10. 1016/j.jcp.2016.12.034.
- [20] P. Schwartz, M. Barad, P. Colella, and T. Ligocki, A Cartesian grid embedded boundary method for the heat equation and Poisson's equation in three dimensions, Comput. Phys., vol. 211, no. 2, pp. 531–550, 2006. DOI: 10.1016/j.jcp.2005.06.010.
- [21] G. Dakin, B. Despres, and S. Jaouen, Inverse lax-Wendorff boundary treatment for compressible Lagrange-remap hydrodynamics on Cartesian grids, Comput. Phys., vol. 353, pp. 228–257, 2018. DOI: 10.1016/j.jcp.2017.10.014.
- [22] P. Colella, D. T. Graves, B. J. Keen, and D. Modiano, A Cartesian grid embedded boundary method for hyperbolic conservation laws, Comput. Phys., vol. 211, no. 1, pp. 347–366, 2006. DOI: 10.1016/j.jcp.2005.05.026.
- [23] R. Crockett, P. Colella, and D. Graves, A Cartesian grid embedded boundary method for solving the Poisson and heat equations with discontinuous coefficients in three dimensions, Comput. Phys., vol. 230, no. 7, pp. 2451–2469, 2011. DOI: 10. 1016/j.jcp.2010.12.017.
- [24] P. McCorquodale, P. Colella, and H. Johansen, A Cartesian grid embedded boundary method for the heat equation on irregular domains, Comput. Phys., vol. 173, no. 2, pp. 620–635, 2001. DOI: 10.1006/jcph.2001.6900.
- [25] H. Johansen, and P. Colella, A Cartesian grid embedded boundary method for Poisson's equation on irregular domains, Comput. Phys., vol. 147, no. 1, pp. 60–85, 1998. DOI: 10.1006/jcph.1998.5965.
- [26] J. B. Angel, J. W. Banks, and W. D. Henshaw, High-order upwind schemes for the wave equation on overlapping grids: Maxwell's equations in second-order form, Comput. Phys., vol. 352, pp. 534–567, 2018. DOI: 10.1016/j.jcp.2017.09.037.
- [27] H. Uddin, R. Kramer, and C. Pantano, A Cartesian-based embedded geometry technique with adaptive high-order finite differences for compressible flow around complex geometries, Comput. Phys., vol. 262, pp. 379–407, 2014. DOI: 10.1016/j.jcp. 2014.01.004.
- [28] A. Main, and G. Scovazzi, The shifted boundary method for embedded domain computations. part i: Poisson and stokes problems, Comput. Phys., vol. 372, pp. 972–995, 2018. DOI: 10. 1016/j.jcp.2017.10.026.
- [29] T. Song, A. Main, G. Scovazzi, and M. Ricchiuto, The shifted boundary method for hyperbolic systems: Embedded domain computations of linear waves and shallow water flows, Comput. Phys., vol. 369, pp. 45–79, 2018. DOI: 10.1016/j.jcp.2018.04.052.
- [30] S. Hosseinverdi, and H. F. Fasel, An efficient, high-order method for solving Poisson equation for immersed boundaries: Combination of compact difference and multiscale multigrid



- methods, Comput. Phys., vol. 374, pp. 912-940, 2018. DOI: 10. 1016/j.jcp.2018.08.006.
- [31] Q. Zhang, and I. Babuska, A stable generalized finite element method (SGFEM) of degree two for interface problems, Comput. Methods Appl. Mech. Eng., vol. 363, pp. 112889, 2020. DOI: 10.1016/j.cma.2020.112889.
- B. Wang, K. Xia, and G.-W. Wei, Second order method for solving 3d elasticity equations with complex interfaces, J. Comput. Phys., vol. 294, pp. 405-438, 2015. DOI: 10.1016/j.jcp. 2015.03.053.
- [33] R. Guo, T. Lin, and Y. Lin, Approximation capabilities of immersed finite element spaces for elasticity interface problems, Numer. Methods Partial Differential Eq., vol. 35, no. 3, pp. 1243-1268, 2019. DOI: 10.1002/num.22348.
- [34] T. H. Huang, J. S. Chen, M. R. Tupek, F. N. Beckwith, J. J. Koester, and H. E. Fang, A variational multiscale immersed meshfree method for heterogeneous materials, Comput. Mech., vol. 67, no. 4, pp. 1059-0924, 2021. DOI: 10.1007/s00466-020-01968-1.
- [35] A. Idesman, and B. Dey, Compact high-order stencils with optimal accuracy for numerical solutions of 2-D time-independent elasticity equations, Comput. Methods Appl. Mech. Eng., vol. 360, pp. 112699, 2020. DOI: 10.1016/j.cma.2019.112699.
- [36] A. Idesman, and B. Dey, Optimal local truncation error method for solution of wave and heat equations for heterogeneous materials with irregular interfaces and unfitted Cartesian meshes, Comput. Methods Appl Mech. Eng., vol. 384, pp. 113998, 2021. DOI: 10.1016/j.cma.2021.113998.
- A. Idesman, and B. Dey, The treatment of the Neumann [37] boundary conditions for a new numerical approach to the solution of PDEs with optimal accuracy on irregular domains and Cartesian meshes, Comput. Methods Appl. Mech. Eng., vol. 365, pp. 112985, 2020. DOI: 10.1016/j.cma.2020.112985.
- [38] A. Idesman, and B. Dey, A new numerical approach to the solution of the 2-D Helmholtz equation with optimal accuracy on irregular domains and Cartesian meshes, Comput. Mech., vol. 65, no. 4, pp. 1189-1204, 2020. DOI: 10.1007/s00466-020-01814-4.

- A. Idesman, A new numerical approach to the solution of [39] PDEs with optimal accuracy on irregular domains and Cartesian meshes. Part 1: The derivations for the wave, heat and Poisson equations in the 1-D and 2-D cases, Arch. Appl. Mech., vol. 90, no. 12, pp. 2621-2628, 2020. DOI: 10.1007/ s00419-020-01744-w.
- B. Dey, and A. Idesman, A new numerical approach to the solution of PDEs with optimal accuracy on irregular domains and Cartesian meshes. Part 2: Numerical simulation and comparison with FEM, Arch. Appl. Mech., vol. 90, no. 12, pp. 2649-2674, 2020. DOI: 10.1007/s00419-020-01742-v.
- A. Idesman, and B. Dey, A new 3-D numerical approach to the solution of PDEs with optimal accuracy on irregular domains and Cartesian meshes, Comput. Methods Appl. Mech. Eng., vol. 354, pp. 568-592, 2019. DOI: 10.1016/j.cma.2019.05.049.
- A. Idesman, and B. Dey, The use of the local truncation error [42] for the increase in accuracy of the linear finite elements for heat transfer problems, Comput. Methods Appl. Mech. Eng., vol. 319, pp. 52-82, 2017. DOI: 10.1016/j.cma.2017.02.013.
- [43] K. J. Bathe, Finite Element Procedures, Prentice-Hall Inc., Upper Saddle River, NJ, 1996.
- [44] H. P. Langtangen, and S. Linge, Finite Difference Computing with PDEs, Springer, Berlin, Germany, 2017.
- T. Lin, D. Sheen, and X. Zhang, A locking-free immersed finite [45] element method for planar elasticity interface problems, Comput. Phys., vol. 247, pp. 228-247, 2013. DOI: 10.1016/j.jcp. 2013.03.053.
- A. Idesman, and B. Dey, New 25-point stencils with optimal [46] accuracy for 2-D heat transfer problems. Comparison with the quadratic isogeometric elements, Comput. Phys., vol. 418, pp. 109640, 2020. DOI: 10.1016/j.jcp.2020.109640.
- [47] A. Idesman, and B. Dey, Accurate numerical solutions of 2-D elastodynamics problems using compact high-order stencils, Comput. Struct., vol. 229, pp. 1-18, 2020. DOI: 10.1016/j.compstruc.2019.106160.

Appendix A.: The coefficients $b_{1,p}$ used in Eq. (24) for the first stencils with j=1

The first 10 coefficients $b_{1,p}$ (p=1,2,...,10) used in Eq. (24) are presented below. All coefficients $b_{1,p}$ used in these formulas are given in the attached file 'b-coef.nb'. For simplicity of notations below, we use that

$$b_{1,i} = b_i (i=1,2,...,10), \quad k_{1,i} = k_i, \; \bar{k}_{1,i} = \bar{k}_i, \; (i=1,2,...,9),$$

$$q_{1,i} = q_i, \; q_{2,i} = q_{i+5}, \; q_{3,i} = q_{i+10}, \; q_{4,i} = q_{i+15}, \; (i=1,2,...,5).$$

$$b_1 = a_1k_1 + a_2k_2 + a_3k_3 + a_4k_4 + a_5k_5 + a_6k_6 + a_7k_7 + a_8k_8 + a_9k_9 + q_1 + q_2 + q_3 + q_4 + q_5$$

$$b_2 = a_1\bar{k}_1 + a_2\bar{k}_2 + a_3\bar{k}_3 + a_4k_4 + a_5\bar{k}_5 + a_6k_6 + a_7k_7 + a_8k_8 + a_9k_9 + q_{11} + q_{12} + q_{13} + q_{14} + q_{15}$$

$$b_3 = -a_1k_1 - a_2k_2 - a_3k_3 - a_4k_4 - a_5k_5 + a_6k_6 - a_7k_7 - a_8k_8 - a_9k_9 + k_1 + k_2 + k_3 + k_4 + k_5 + k_6 + k_7 + k_8 + k_9 - q_1 - q_2 - q_3 - q_4 - q_5$$

$$b_4 = -a_1\bar{k}_1 - a_3\bar{k}_2 - a_3\bar{k}_3 - a_4k_4 - a_5k_5 - a_6k_6 - a_7k_7 - a_8k_8 - a_9k_9 + k_1 + k_2 + k_3 + k_4 + k_5 + k_6 + k_7 + k_8 + k_9 - q_{11} - q_{12} - q_{13} - q_{14} - q_{15}$$

$$b_5 = -a_1\bar{k}_1 + a_3k_3 - a_4k_4 + a_6k_6 - a_7k_7 + a_9k_9 + d_{x_1}q_1 + d_{x_2}q_2 + d_{x_3}q_3 + d_{x_4}q_4 + d_{x_5}q_5 + \lambda_8n_{x_1}q_6$$

$$+ \lambda_8n_{x_2}q_7 + \lambda_8n_{x_3}q_8 + \lambda_8n_{x_4}q_9 + \lambda_8n_{x_3}q_{10} + \lambda_8n_{y_1}q_{16} + \lambda_8n_{y_2}q_{17} + \lambda_8n_{y_3}q_{18} + \lambda_8n_{y_4}q_{19} + \lambda_8n_{y_5}q_{20} + 2n_{x_1}n_4q_6$$

$$+ 2n_{x_2}\mu_4q_7 + 2n_{x_3}\mu_4q_8 + 2n_{x_4}\mu_4q_9 + 2n_{x_5}\mu_4q_{10}$$

$$b_6 = -a_1\bar{k}_1 + a_3k_3 - a_4\bar{k}_4 + a_6k_6 - a_7k_7 + a_9k_9 + d_{x_1}q_{11} + d_{x_2}q_{12} + d_{x_3}q_{13} + d_{x_4}q_{14} + d_{x_5}q_{15} + n_{x_1}\mu_4q_6$$

$$+ n_{x_2}\mu_4q_7 + 2n_{x_3}\mu_4q_18 + n_{x_4}\mu_4q_9 + n_{x_5}\mu_4q_{20} + n_{y_1}\mu_4q_6 + n_{y_2}\mu_4q_7 + n_{y_3}\mu_4q_8 + n_{y_4}\mu_4q_9 + n_{y_5}\mu_4q_{10}$$

$$b_7 = (a_1 - 1)k_1 - a_3k_3 + a_4k_4 - a_6k_6 + a_7k_7 - a_9k_9 - d_{x_1}q_1 - d_{x_2}q_2 - d_{x_3}q_3 - d_{x_4}q_4 - d_{x_5}q_5 - \lambda_8n_{x_1}q_6 - \lambda_8n_{x_2}q_7 - \lambda_8n_{x_3}q_{18} - \lambda_8n_{x_4}q_9 - \lambda_8n_{x_3}q_{18} - \lambda_8n_{x_4}q_9 - \lambda_8n_{x_3}q_{19} - \lambda_8n_{x_3}q_$$